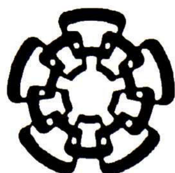

CENTRO DE INVESTIGACIÓN Y DE ESTUDIOS AVANZADOS DEL INSTITUTO POLITÉCNICO NACIONAL

UNIDAD QUERÉTARO

CELDAS SOLARES DE HETEROUNIÓN BASADAS EN EL CUATERNARIO CuCdTeO FABRICADAS A TEMPERATURA AMBIENTE

Tesis que presenta

Alejandro Gojon Montañez

para obtener el Grado de

Maestro en Ciencias

en la Especialidad de

Materiales

CINVESTAV
IPN
ADQUISICION
LIBROS

Director de tesis:

Dr. Sergio Joaquín Jiménez Sandoval

Santiago de Querétaro, Qro. Septiembre 2015

CLASIF.. CQ 00264
ADQUIS.. CQ-280-SS1
FECHA: 24-Mayo-2016
PROCED.. Don. 2016
$
D: 226314-100

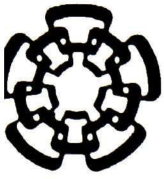

CENTRO DE INVESTIGACIÓN Y DE ESTUDIOS AVANZADOS DEL INSTITUTO POLITÉCNICO NACIONAL

UNIDAD QUERÉTARO

HETEROJUNCTION SOLAR CELLS BASED ON THE QUATERNARY CuCdTeO FABRICATED AT ROOM TEMPERATURE

Thesis presented by

Alejandro Gojon Montañez

to obtain the Grade of

Master of Science

with a major in

Materials

Thesis assessor:

Dr. Sergio Joaquín Jiménez Sandoval

Santiago de Querétaro, Qro. September 2015

Acknowledgements.

The culmination of this entire piece couldn´t been achieved without the constant support of my four parents, Claudia Montañez, Erika Garza, Héctor Gojon and Luis Moncada.

This work is entirely dedicated to my sister and brothers María José Moncada, Héctor and Marcelo Gojon.

I wish to honor the memory of Alejandro Iván González Casanova, who left his earthly bound state before this assignment was fulfilled.

To my enduring tutor over the last couple of years Bárbara Muñiz.

To my thesis committee consisting of Sergio Jiménez, Arturo Mendoza and Rebeca Castanedo, whose constant inquiries drove me along the knowledge aisle.

I wish to acknowledge the invariable technical support by Cyntia Zúñiga, Francisco Rodríguez, Martín Hernández, Joaquín Márquez, Gerardo Torres, Edgar Cruz, Christian Enríquez, Adair Jiménez, Eleazar Urbina, Eleazar León and Marco Trejo.

Funding by CONACYT-Mexico was imperative to fulfill the current work.

On commemorating the International Year of Light and Light-based Technologies, the 50th anniversary of the Grateful Dead, and of course, my M. Sc. dissertation:

Sometimes the lights all shining on me,
Other times I can barely see;
Lately it occurs to me,
What a long, strange trip has been.

— From the song "*Truckin'*", by the Grateful Dead.

Contents.

Acknowledgements.................................... v
Abstract.................................... ix
Resumen.................................... x
List of figures.................................... xi
List of tables.................................... xiii

1. Introduction.................................... 1

2. Objectives.................................... 3
  2.1. General objective.................................... 3
  2.2. Specific objectives.................................... 3
  2.3. Goals.................................... 3

3. Background.................................... 5
  3.1. Photovoltaic technology.................................... 5
  3.2. Thin-film solar cells.................................... 11
  3.3. Cadmium telluride and copper oxide alloys.................................... 13
  3.4. Zinc oxide.................................... 15

4. Fabrication and characterization details.................................... 19
  4.1. RF magnetron sputtering.................................... 19
  4.2. Topography and morphology.................................... 21
    4.2.1. Mechanical profilometry.................................... 21
    4.2.2. Optical profilometry.................................... 22
    4.2.3. Electron microscopy.................................... 22
    4.2.4. Atomic force microscopy.................................... 23
  4.3. Structural properties.................................... 24
    4.3.1. X-ray diffraction.................................... 24
    4.3.2. Raman scattering.................................... 28
  4.4. Optical properties.................................... 31
  4.5. Electrical properties.................................... 33
    4.5.1. Hot-point probe method.................................... 33
    4.5.2. Hall effect.................................... 34
    4.5.3. Electron work function.................................... 38
  4.6. Band offset at junctions.................................... 39
  4.7. Solar cell performance.................................... 42

5. Experimental details.................................... 47
  5.1. CCTO thin films.................................... 47
  5.2. Cu front contact.................................... 47
  5.3. ZnO thin films.................................... 48
  5.4. Ti/Al contact.................................... 48

6. Results and discussion. 49
6.1. CCTO thin films. 49
6.1.1. Topography. 49
6.1.2. Morphology. 51
6.1.3. Chemical composition. 52
6.1.4. Structural characterization. 53
6.1.4.1. X-ray diffraction. 53
6.4.1.2. Raman scattering. 56
6.1.5. Optical characterization. 57
6.1.6. Electrical characterization. 61
6.1.6.1. Hot-point probe. 61
6.1.6.2. Work function. 62
6.2. Cu front contact. 63
6.2.1. Cu/*p*-CCTO junction 63
6.2.2. Thickness. 63
6.2.3. Electrical characterization. 64
6.3. ZnO thin films. 65
6.3.1. Topography. 65
6.3.2. Morphology. 66
6.3.3. Structural characterization. 67
6.3.3.1. X-ray diffraction. 67
6.3.3.2. Raman scattering. 68
6.3.4. Optical characterization. 68
6.3.5. Electrical characterization. 69
6.3.5.1. Work function. 70
6.4. Ti/Al contact. 71
6.4.1. *n*-ZnO/Ti/Al junction. 71
6.4.2. Thickness. 71
6.4.3. Electrical characterization. 72
6.5. Heterojunction. 72
6.5.1. *p*-CCTO/*n*-ZnO. 72
6.6. Heterojunction solar cell. 73
6.6.1 Efficiency. 73

7. Closure. 79
7.1. Conclusions. 79
7.1.1. CCTO thin films: absorbing layer. 79
7.1.2. ZnO thin films: window layer. 80
7.1.3. Heterojunction solar cells. 81
7.2. Perspectives. 81

Abstract.

Heterojunction superstrate-type solar cells were fabricated at room temperature by radiofrequency magnetron sputtering. CdTe + CuO (CCTO) and ZnO targets were used for the base and emitter layers deposition, respectively. The surface roughness values of the CCTO thin films were measured with a maximum value of 4.30 nm. The chemical analysis results showed inverse tendencies for the Cu and Cd elemental compositions. Through X-ray diffraction, preferential orientations were found for the CCTO samples on the [111]c/[002]h, [100]h and [220]c/[110]h directions of the cubic and hexagonal phases of the CdTe host. Diffraction peaks of Cu_2Te, $Cu_{2.72}Te$ and $CdTeO_3$ were found to a lesser extent. The LO and 2LO phonon modes of cubic CdTe were found for all the CCTO samples except for CCTO25, in which a wide band appeared within the range of theoretically calculated vibrational modes of Cu_2Te (< 200 cm^{-1}). Evidence of the E_1 and $E_1 + \Delta_1$ critical points of cubic CdTe was found in the reflectance spectra of the samples. Band gap values varied from 1.76 for CdTe to 1.45 eV for CCTO25. Hot-point probe characterization proved *n*-type conductivity for CCTO0-9 samples and *p*-type conductivity for CCTO10-25. Electron work function values were obtained ranging from 4.73 to 6.38 eV. Cu was used as ohmic contacs to the CCTO films. The maximum hole concentration as measured by Hall effect was $2.4\text{x}10^{20}$ cm^{-3} for CCTO15 and a minimum resistivity of $2.44\text{x}10^{-2}$ Ω·cm for CCTO25. The surface roughness of the Zno thin film was measured as 2.37 nm. Preferred orientation on the [002]h direction of the hexagonal zincite phase was found through X-ray diffraction, and the crystallite size was calculated as 104 Å. Optical spectroscopy results showed 80% of transmittance and 15% of reflectance of the ZnO thin film. The band gap value was calculated as 3.27 eV. The work function of ZnO was measured as 4.0 eV. Ti and Al were used as ohmic contacs to the ZnO films. The electron concentration was $1.71\text{x}10^{19}$ cm^{-3} with a resistivity value of $1.09\text{x}10^{-1}$ Ω·cm for the as-deposited ZnO thin film. The efficiency values of the *p*-CCTO/*n*-ZnO solar cells under air mass 1.5 global illumination were measured within the range of 10^{-4} - 10^{-6} %, with no evident changes after soft thermal treatments.

Resumen.

Se fabricaron celdas solares de heterounión de tipo superestrato por erosión catódica de radiofrecuencia a temperatura ambiente. Se utilizaron blancos de CdTe + CuO (CCTO) y ZnO para el depósito de las capas base y emisora, respectivamente. Valores de rugosidad superficial de películas delgadas de CCTO fueron medidas con un máximo de 4.30 nm. El análisis químico de las películas reveló tendencias inversas para las composiciones elementales de Cu y Cd. Por medio de difracción de rayos-X se encontraron orientaciones preferenciales en las direcciones [111]c/[002]h, [100]h y [220]c/[110]h de las fases cúbica y hexagonal de CdTe. Se encontraron picos de difracción de baja intensidad debidos a Cu_2Te, $Cu_{2.72}Te$ y $CdTeO_3$. Los modos LO y 2LO de CdTe cúbico fueron encontrados para todas las muestras de CCTO excepto para CCTO25, en la cual apareció una banda ancha dentro del rango de los modos vibracionales teóricos de Cu_2Te ($< 200 cm^{-1}$). Se encontró evidencia de los puntos críticos E_1 y $E_1 + \Delta_1$ de CdTe cúbico en los espectros de reflectancia de las muestras de CCTO. Los valores de energía del ancho de banda prohibida oscilaron entre 1.76 para CdTe y 1.45 eV para CCTO25. La caracterización por punta caliente demostró conductividad tipo *n* para las CCTO0-9 y tipo *p* para CCTO10-25. Los valores de la función de trabajo medidos variaron entre 4.73 y 6.38 eV. Se utilizó Cu como contacto óhmico sobre películas de CCTO. La máxima concentración de huecos medida por efecto Hall fue de $2.4x10^{20}$ cm^{-3} para CCTO15 y una resistividad mínima de $2.44x10^{-2}$ $\Omega \cdot cm$ para CCTO25. El valor de rugosidad superficial de películas de ZnO fue de 2.37 nm. Se encontraron orientaciones preferenciales sobre la dirección [002]h de la estructura zincita de ZnO y se calculó el tamaño de cristalito de 104 Å. Los resultados de espectroscopia óptica mostraron 80% de transmitancia y 15% de reflectancia. El valor de energía del ancho de banda prohibida fue calculado como 3.27 eV. La función de trabajo de muestras de ZnO fue de 4 eV. Ti y Al fueron usados como contactos óhmicos sobre películas de ZnO. La concentración de electrones fue de $1.71x10^{19}$ cm^{-3} y una resistividad de $1.09x10^{-1}$ $\Omega \cdot cm$. Los valores de eficiencia de celdas solares *p*-CCTO/*n*-ZnO fueron medidas bajo iluminación *air mass 1.5 global*, obteniendo valores dentro del rango $10^{-6} - 10^{-4}$ %, sin cambios evidentes después de tratamientos térmicos suaves.

List of figures.

Figure 3.1. Solid state devices. (a) PV and (b) PE effects.... 5
Figure 3.2. Flat band schemes. (a) Metal, (b) intrinsic semiconductor and (c) insulator.................................. 6
Figure 3.3. Flat bands of extrinsic semiconductors. (a) *p*-type and (b) *n*-type semiconductors........................... 8
Figure 3.4. Short-circuited solar cell under illumination..... 8
Figure 3.5. Solar spectral irradiance......................... 9
Figure 3.6. J-V curve of a Si homojunction solar cell........ 10
Figure 3.7. Research solar cells efficiency track............ 12
Figure 3.8 CdTe polytypes. (a) Zincblende, (b) Zincite....... 13
Figure 3.9. Zincblende CdTe electron band structure.......... 15
Figure. 3.10. ZnO polytypes. (a) Rocksalt, (b) Zincite and (c) Zincblende... 16
Figure 3.11. Zincite ZnO electronic band structure........... 17
Figure 4.1. Sputtering system scheme......................... 19
Figure 4.2. Franky sputtering system......................... 21
Figure 4.3. Stylus profilometry.............................. 21
Figure 4.4. Optical profilometry............................. 22
Figure 4.5. EPMA sample holder............................... 23
Figure 4.6. KPFM measurement................................. 24
Figure 4.7. Bragg reflection................................. 26
Figure 4.8. Calibration Si diffraction pattern............... 27
Figure 4.9. X-ray diffraction measurement.................... 28
Figure 4.10. Phonon absorption and emission.................. 29
Figure 4.11. Reference Si Raman spectrum..................... 30
Figure 4.12. Raman scattering measurement.................... 30
Figure 4.13. Light-matter interaction phenomena.............. 31
Figure 4.14. Glass substrate R and T measurement............. 33
Figure 4.15. Reference Si wafers potential differences....... 34
Figure 4.16. Hot-point probe system.......................... 34
Figure 4.17. Hall effect geometry............................ 35
Figure 4.18. Hall Effect characterization.................... 37
Figure 4.19. I-V curve by 4-point probe method............... 37
Figure 4.20. Metal/*p*-semiconductor junction. (a) Before and (b) after contact... 40
Figure 4.21. *n*-semiconductor/metal junction. (a) Before and (b) after contact... 41
Figure 4.22. *p-n* heterojunction. (a) Before and (b) after contact.. 41
Figure 4.23. Illuminated solar cell electrical model......... 42

Figure 4.24. Solar cell performance measurement configuration 43
Figure 4.25. Si solar cell performance 44
Figure 4.26. Efficiency measurement 45
Figure 6.1. Base layer 3-D design. (a) Thickness and (b) distribution 49
Figure 6.2. Topographical maps.(a) CCTO0, (b) CCTO10 and (c) CCTO25 50
Figure 6.3. Morphological maps.(a) CCTO0, (b) CCTO10 and (c) CCTO25 51
Figure 6.4. CCTO films elemental composition trends 52
Figure 6.5. CCTO samples X-ray diffraction patterns 53
Figure 6.6. Some crystallographic planes in wurtzite structure 55
Figure 6.7. Some crystallographic planes in zincblende structure 55
Figure 6.8. CCTO films Raman spectra 56
Figure 6.9. CCTO samples reflectance spectra 57
Figure 6.10. Cubic CdTe critical points in CCTO reflectance spectra 58
Figure 6.11. Translucent CCTO samples transmittance spectra ..58
Figure 6.12. CCTO samples fundamental edges of absorption 59
Figure 6.13. CCTO samples UV-VIS-NIR transmittance spectra ...60
Figure 6.14. CCTO samples fundamental edges of absorption 60
Figure 6.15. CCTO hot-point probe potential differences 61
Figure 6.16. CCTO thin films work functions 62
Figure 6.17. Cu/*p*-CCTO junction. (a) Before and (b) after contact 63
Figure 6.18. CCTO Hall effect samples 3-D design. (a) Cross-sectional and (b) planar views 63
Figure 6.19. CCTO films resistivity and majority charge carrier concentration 65
Figure 6.20. CCTO films conductivity and mobility 65
Figure 6.21. Window layer 3-D design. (a) Thickness and (b) geometry 66
Figure 6.22. ZnO topographical map. (a) 2-D and (b) 3-D view .66
Figure 6.23. ZnO ESEM morphology 66
Figure 6.24. ZnO film X-ray diffraction pattern 67
Figure 6.25. Zincite [002]h preferred orientation. (a) planar and (b) lateral views 67
Figure 6.26. ZnO sample Raman frequencies 68
Figure 6.27. ZnO film reflectance and transmittance spectra ..69
Figure 6.28. ZnO sample fundamental edge of absorption and linear fit to determine E_g 69

Figure 6.29. ZnO film hot-point probe voltage as a function of time.... 70
Figure 6.30. Contact potential difference images. (a) Gold and (b) ZnO thin film.... 70
Figure 6.31. *n*-ZnO/Ti junction. (a) Before and (b) after contact.... 71
Figure 6.32. ZnO Hall effect samples 3-D design. (a) Laterial and (b) planar views.... 71
Figure 6.33. *p*-CCTO/*n*-ZnO heterojunction. (a) Before and (b) after contact.... 72
Figure 6.34. Configuration #1 solar cells. (a) Lateral and (b) planar views.... 73
Figure 6.35. Configuration #1 solar cell thickness values.... 73
Figure 6.36. Configuration #2 solar cells 3-D design. (a) Lateral and (b) planar views.... 73
Figure 6.37. Configuration #2 solar cell lateral view scheme. 74
Figure 6.38. CCTO10 solar cell J-V under illumination.... 74
Figure 6.39. CCTO11 solar cell J-V under illumination.... 75
Figure 6.40. CCTO12 solar cell J-V under illumination.... 75
Figure 6.41. CCTO13 solar cell J-V under illumination.... 75
Figure 6.42. CCTO14 solar cell J-V under illumination.... 76
Figure 6.43. CCT015 solar cell J-V under illumination.... 76
Figure 6.44. CCTO20 solar cell J-V under illumination.... 76
Figure 6.45. CCTO25 solar cell J-V under illumination.... 77

List of tables.

Table 4.1. Components.... 19
Table 5.1. CCTO thin films deposition times.... 47
Table 6.1. CCTO films elemental composition analysis.... 52
Table 6.2. CCTO samples vibrational dynamics.... 57
Table 6.3. CCTO films band gaps.... 59
Table 6.4. CCTO films band gaps.... 61
Table 6.5. CCTO samples work functions.... 62
Table 6.6. CCTO samples electrical parameters.... 64
Table 6.7. ZnO films Raman frequencies.... 68
Table 6.8. Electrical parameters of ZnO thin films.... 72
Table 6.9. *p*-CCTO/*n*-ZnO junction barrier height.... 72
Table 6.10. Heterojunction CCTO-based solar cell parameters.. 74

1. Introduction.

Sun is the leading source of energy in our planetary system. By means of natural fusion: protons and electrons merging together to form heavier elements, constant ionizing and non-ionizing electromagnetic radiation is generated jointly with solar winds of charged and neutral particles. Massive amounts of ultraviolet, visible, and infrared radiation arrive to the surface of the third closest planet orbiting this star. These incident wave packets interact with the materials on Earth´s surface and atmosphere producing effects such as coloration, heat, ionization, reflection, photoelectricity and more light-matter interaction phenomena.

During the last half century humanity has been developing technology to take advantage of the renewable and self-sustaining solar energy. This led to constant research on more efficient materials for the proper energy conversion: from constant emission of photons by the sun to the generation of direct current of electrons by the device. Through theoretical calculations or experimental evidence, scientists from labs all over the globe pursue a common goal. This is, to construct efficient research solar cells from abundant materials with the aim on evolving into a functional photovoltaic module or solar panel. This science-industry enterprise must resolve into low-cost fabrication in large scale and to sustain a competent efficiency per module, compared to the expensive lab procedures and high research-cell efficiencies.

Recent progress on tailoring the properties of semiconducting thin films had led photovoltaic-related research groups to investigate the full scope that thin-film solar cells can provide as an economic and environmental friendly solution to energy problems.

With the latter in mind, the present work exhibits the fabrication and characterization of thin-film heterojunction solar cells based on the semiconducting materials cadmium telluride doped with copper oxide (CuCdTeO) and zinc oxide (ZnO).

Chapter two exposes the objectives and goals to accomplish during the development of this work. The phenomenon of direct conversion of light into electricity by a solar cell and the relevant properties of the involved materials are presented in Chapter 3. Chapter 4 exposes relevant information about the fabrication and characterization techniques for each layer composing the thin-film heterojunction solar cells and for the device itself. The main details on the fabrication of the thin films involved in the superstrate-type solar cell are described in Chapter 5. Chapter 6 exhibits the characterization results, altogether with discussions about the reported properties. Conclusions and perspectives for future works are listed in Chapter 7.

2. Objectives.

2.1. General objective.

2.1.1. To determine the properties of solar cells of the type ZnO/CuCdTeO fabricated at room temperature and determine the effect of the concentrations of copper, oxygen and of thermal treatments on their efficiency.

2.2. Specific objectives.

2.2.1. To fabricate thin films of CuCdTeO by RF sputtering at room temperature starting from targets made from CdTe and CuO powders varying the concentration of CuO.

2.2.2. To determine the structural, optical and electrical properties of the CuCdTeO films as a function of the concentration of CuO in the target.

2.2.3. To fabricate ZnO thin films by RF sputtering at room temperature on glass substrates.

2.2.4. To determine the structural, optical and electrical properties of the ZnO films.

2.2.5. To fabricate ZnO/CuCdTeO solar cells using targets made from CdTe and CuO powders for the chosen concentrations of CuO.

2.2.6. To evaluate the performance of the ZnO/CuCdTeO solar cells fabricated at room temperature.

2.2.7. To evaluate the effect of thermal treatments in air on the performance of the ZnO/CuCdTeO solar cells.

2.3. Goals.

2.3.1. To grow CuCdTeO thin films by RF sputtering on glass substrates and to evaluate the electrical characteristics of contacts of Cu on this material as a function of the concentration of CuO in the target.

2.3.2. To grow Zno thin films by RF sputtering on glass substrates and evaluate the electrical characteristics of metallic contacts on this material.

2.3.3. To fabricate glass/contact/ZnO/CuCdTeO/Cu solar cells by RF sputtering at room temperature.

2.3.4. To determine the I-V characteristics of the solar cells in the dark and under illumination.

2.3.5. To determine the efficiency of the solar cells fabricated at room temperature and after being thermally treated in air from 100 °C to 350 °C in 50 °C increments.

3. Background.

3.1. Photovoltaic technology.

The photovoltaic (PV) effect was first reported in 1839 by E. Becquerel. He documented the generation of constant current of electrons through the absorption of radiating energy (visible light) by an electrolytic cell with distinct metallic electrodes. W. Adams and R. Day observed the PV effect with solid selenium (Se) until 1877. The mathematical approach to the PV understanding was provided by A. Einstein in 1905 by modeling the photoelectric (PE) effect. In the latter, the energized electrons leave behind the solid under ionizing illumination (ultraviolet light), as reported by H. Hertz in 1887. Figure 3.1 depicts the main difference between the two phenomena.

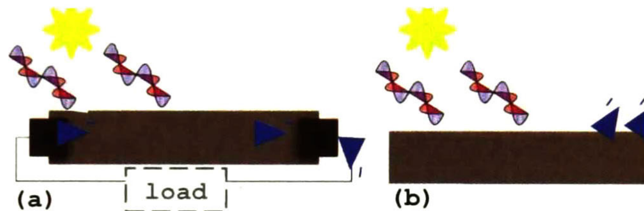

Figure 3.1. Solid state devices. (a) PV and (b) PE effects.

In Figure 3.1(a) are shown excited electrons leaving a device through metallic contacts toward an external circuit and Figure 1(b) shows promoted electrons unto free states in the vacuum (considered as free electrons with mass m_o, described by ordinary wave functions Ψ). Electrons in a pure and crystalline material are quasifree electrons (slower than free electrons) with effective mass m*, described by Bloch wave functions (Ψ_B) that spread throughout the volume of the crystal. These Bloch functions possess information about the periodicity of the atomic nuclei in the rigid structure and differ from those of free electrons or from electrons of atoms in gaseous phase.

At 0 K, all the valence electrons (involved in chemical bonding) within the crystal pack themselves into the lowest energy states by pairs. According to the Pauli Exclusion Principle only two electrons with different quantum numbers can occupy the same energy state. Paired electron wave functions group within the valence band (VB) in three

ensembles (this is the case for solids formed by chemical elements from group 14 in the periodic table or by compounds of elements displaced symmetrically from group 14). These are named (from lower to higher energies) the split-off (SO), the heavy hole (HH) and the light hole (LH) bands.

Beyond the VB highest occupied state a gap in energy exists with no allowed states for electrons (i.e. electrons within the crystal cannot attain stable energy values within this forbidden band). This is called the band gap and its magnitude sets the minimum value of energy that an electron may receive to leave a bound state in the VB (i.e. leaving behind a hole in the lower band). Through optical, electrical or thermal excitations electrons can leave behind lower energy states in the VB, onward to higher energy states in the upper available bands.

Across the band gap, higher energy bands exist named electron bands together assembling the overall conduction band (CB). This upper band contains available states for the electrons to occupy after their VB-to-CB transitions through the band gap. The spatial distribution of electrons and holes in the VB and the CB is set by the symmetry of the crystal lattice of the solid. A general representation consists of the flat band schemes shown in Figure 3.2.

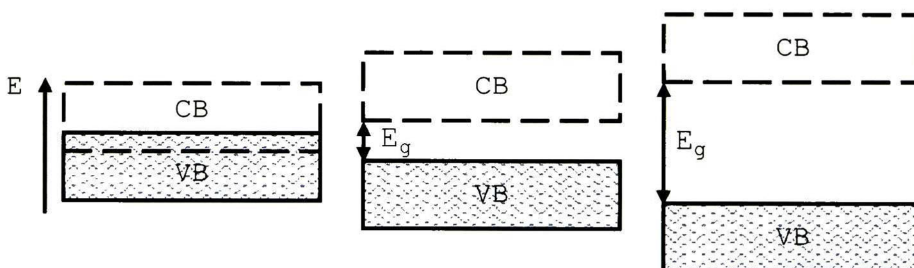

Figure 3.2. Flat band schemes. (a) Metal, (b) intrinsic semiconductor and (c) insulator.

Figure 3.2(a) depicts the band overlap found in metallic materials, recognized for their feasible conduction of electricity even at low temperatures near 0 K. Through this overlap (no band gap) electrons involved in the metallic bonding of the crystal are easily excited to move freely and conduct electricity and heat. Common values of resistivity (capacity of a material to oppose to the flow of electrons throughout its volume) for metals at room temperature (RT) are

of the order of 10^{-6} Ω·cm. Insulators, on the other hand, possess a wide band gap, with magnitudes around 10 eV. Insulating materials do not conduct electricity and possess values of resistivity greater than 10^{7} Ω·cm. Figure 3.2(c) illustrates the wide separation between the VB maximum and CB minimum for an insulating material.

Semiconducting materials present electrical behavior between metals and insulators. Semiconductors can be as resistive as an insulator at low temperatures and nearly as conductive as metals at RT conditions. These materials can be classified into two main categories: intrinsic and extrinsic semiconductors. Figure 3.2(b) depicts the flat band diagram for an intrinsic semiconductor. Electrical conduction in intrinsic semiconductors is possible through the motion of electrons in the CB (in a given direction set by an electric field) and holes in the VB (in the opposite direction). In extrinsic semiconductors a given charge carrier is the responsible for the electrical conduction, i.e. by electrons in the CB or by holes in the VB. These are named *n*-type and *p*-type semiconductors, respectively.

Extrinsic semiconductors can be obtained by doping an intrinsic semiconductor (element from group 14 such as Si or Ge) with trivalent or pentavalent elements (i.e. with elements from groups 13 or 15, respectively). For a covalent crystal formed by an element of group 14, an atom is able to share 4 electrons of its last quantum level (outer or valence shell) to form stable crystalline arrangements. For *p*-doping (trivalent element) a hole is added to the solid due to the existence of 3 electrons in the valence shell of the impurity atom. This indicates that trivalent atoms within a covalent crystal act as acceptors for thermally excited electrons that belong to the intrinsic semiconductor. Pentavalent impurities, on the other hand, posses 5 electrons in their valence shells, leading to donor behavior within the crystal. Acceptor and donor impurities introduce stable energetic levels within the band gap of the extrinsic semiconductor. These are localized states (as opposed to delocalized Bloch states) due to their implicit localization around the nuclei of their respective impurity atoms. Figure 3.3 shows flat band schemes for two distinct extrinsic semiconductors where $E_g^p \neq E_g^n$.

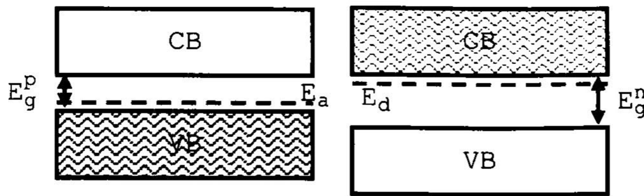

Figure 3.3. Flat bands of extrinsic semiconductors. (a) *p*-type and (b) *n*-type semiconductors.

Figure 3.3(a) depicts the case for *p*-type semiconductors, in which the acceptor energetic states lie close to the VB maximum. In Figure 3.3(b) are illustrated the donor states close to the CB maximum for an *n*-type semiconductor. At 0 K all the valence electrons pack into the lowest energy states and the top limit is set by the acceptor or donor energy states within the gap, for *p*- and *n*-type semiconductors, respectively. Electrons may be trapped by the available holes around acceptor impurities and attain E_a energy values within a *p*-type semiconductor. For an *n*-type semiconductor electrons may be attracted by the unbalanced positive charge of the donor impurity and attain energy values equal to E_d. These energy states are also named Fermi energy levels and set the chemical potential levels for the extrinsic semiconductors.

Solid-state PV technology is based on the junction of two (or more) semiconducting materials, each with an opposite shift of the Fermi energy, i.e. a *p-n* junction. Homo- (same materials and band gaps) and heterojunctions (different materials and band gaps) are encountered among the great number of configurations for research and commercial solar cells. Figure 3.4 illustrates the generation of an electrical current by a heterojunction solar cell under illumination.

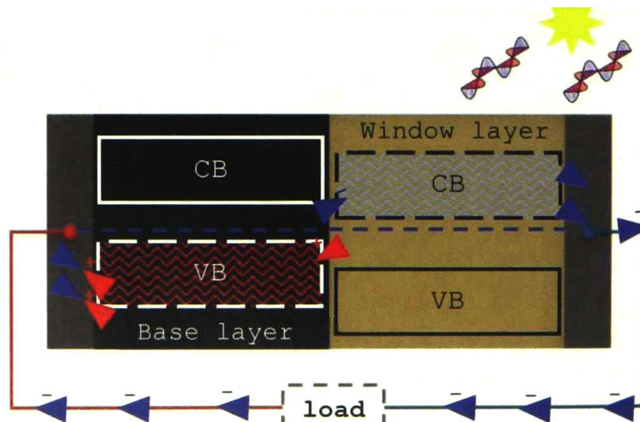

Figure 3.4. Short-circuited solar cell under illumination.

When *p*-type and *n*-type semiconductors are joined, the chemical potential level (at RT) for each material must balance throughout the system, i.e. the *p-n* junction. When electrons diffuse from the *n*-region into the *p*-region, they leave behind positively charged donor atoms. Negatively charged atoms are left behind in the *p*-region when holes diffuse into the *n*-region, due to the occupancy of an electron in the available state introduced by the acceptor impurity. This process of diffusion ceases when the Fermi energy is balanced throughout the junction. Paired with this equilibrium, an electrical phenomenon arises at the junction, which is recognized as the basis of the semiconductor-based technology.

An intrinsic electric field at the junction is created, caused by the oppositely charged impurities within the *p*- and *n*-type semiconductors composing the device. This electric field opposes to further charge carrier diffusion, and establishes a depletion region at the junction, where no ionized impurities are found. This implies that no charge carriers available for electrical conduction are present in the depletion region, leading to an overall change in the electrical properties of the junction. This effect is manifested as a potential barrier between the semiconductors, whose majority charge carriers from either side must overcome to deliver electrical current across the device. Solar light absorption by the *p-n* junction consists of energy supply to surpass the potential barrier. Measured solar irradiance spectra are shown in Figure 3.5.

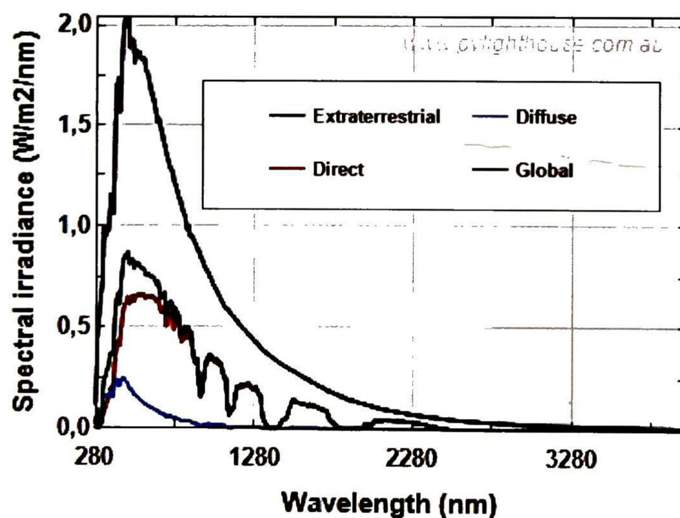

Figure 3.5. Solar spectral irradiance [1].

Knowledge of the light properties and the materials for the generation of electrical energy by means of solar energy absorption is vital for consistent fabrication and study of PV devices. Pioneer solar cells were employed in the outer space to sustain spacecrafts and other Earth-orbiting satellites. Nowadays, PV technology is vastly found in first- and third-world countries, with the aim to be a prime participant in clean power generation within the decades to come.

The spectral response of a solar cell in Earth´s crust is limited by the solar irradiance that overcomes the gas layers of Earth´s atmosphere. A global irradiance is set as the standard illumination for the electrical characterization of research solar cells. PV-related research groups among the global pursue of a common goal: achieve high solar cell power efficiencies through cheap and clean fabrication processes with reproducible results. Imperative high performances of research-size solar cells must be obtained, with the goal to sustain reasonable efficiencies after the industrialization of the device is consummated.

The efficiency (η) of a research-size solar cell is calculated from current density - voltage (J-V) measurements of the *p-n* junction under standardized illumination, namely the air mass 1.5 global (AM1.5G) illumination. Figure 3.6 shows typical J-V relationships for a research solar cell in dark and under illumination. The displacement of the J-V curve when the solar cell is illuminated indicates electrical power generation.

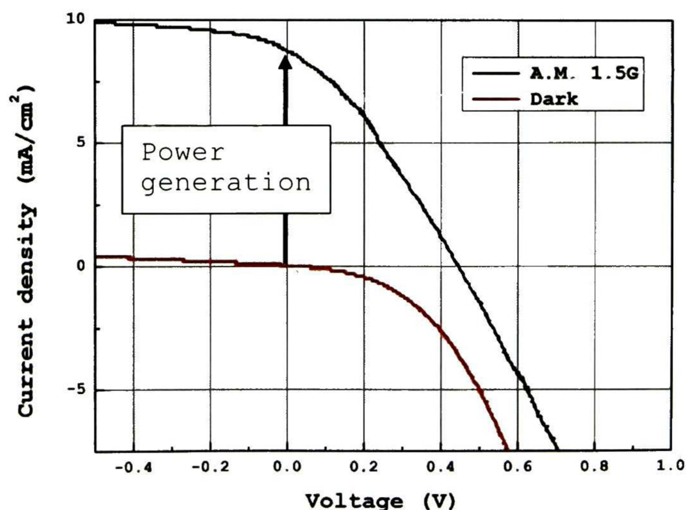

Figure 3.6. J-V curve of a Si homojunction solar cell.

3.2. Thin-film solar cells.

Thin-film technology is a novel method for research and industrialization of micro and nanostructured devices, with rather small amounts of materials. New properties may arise from thin single- or multilayer structures fabricated on standard substrates, apart from the bulk properties of a given material. Thin films of semiconducting materials can be deposited on amorphous, mono- and polycrystalline substrates by means of different growth techniques. High-temperature or RT conditions are employed in order to increase crystalline quality and reduce imperfections and stress generated during deposition.

Typical thickness values for the *n*- and *p*-type regions of thin-film heterojunction solar cells are reported as ~400 nm and ~2 μm, respectively. The thicker film is the absorber or base layer while the thinner film is the emitter or window layer. Solar light propagates across the window layer, and since $E_g^n > E_g^p$, there is (ideally) no light absorption across the *n*-semiconductor and rather occurs at the junction. Light is now able to promote VB-to-CB electronic transitions across a given length within the base layer. Photogenerated electron-hole (e^--h^+) pairs away from the junction may be lost through their recombination. The e^--h^+ pairs generated near the junction are able to split and conduct electricity (in opposite directions). The electron diffuses into the *n*-region and leaves the device through the negative metallic contact. The hole flows toward the positive contact and recombines with a returning electron.

Since the processes of light absorption and generation of utile pairs of charge carriers occur within a very short length, thin-film technology provides a convenient path to solar cell fabrication. In order to save material resources, research-size solar cells are fabricated and studied with the intention of achieving high efficiencies that endure once the solar module is assembled.

The National Renewable Energy Laboratory (NREL) is a leading institution in renewable sources of energy and comprises the track of reported efficiencies for research-size solar cells shown in Figure 3.7. CdTe-based solar cells possess up to 21.5% efficiency by the solar panel manufacturer First Solar.

Figure 3.7. Research solar cells efficiency track [2].

3.3. Cadmium telluride and copper oxide alloys.

Cadmium telluride (CdTe) is a II-IV semiconducting compound, with predominant covalent bonding (due to their low electronegativity difference, where $\chi_{Cd} = 1.52$ and $\chi_{Te} = 2.15$, in the Allen scale). It is an amphoteric semiconductor, which implies unintentional *n*- or *p*-type doping. During the fabrication process vacancies and interstitials of Cd^{2+} ions can be created acting as acceptors and donors, respectively. This covalent compound can be found in two distinct crystalline arrangements as shown in Figure 3.8. Figure 3.8(a) shows the cubic phase of CdTe and Figure 3.8(b) shows the hexagonal structure. Common values of the lattice parameters of the cubic phase are a = b = c = 6.48 Å, and of the hexagonal structure are a = b = 4.58 Å and c = 7.50 Å.

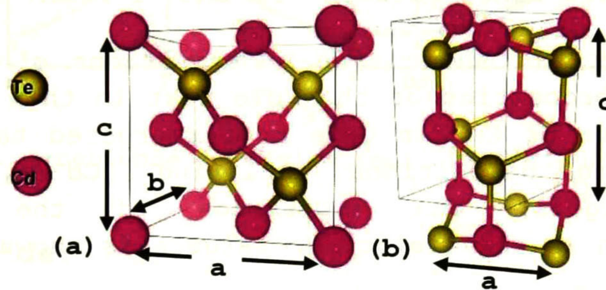

Figure 3.8. CdTe polytypes. (a) Zincblende and (b) wurtzite structures.

This semiconducting compound has been employed as the absorber layer in heterojunction solar cells due to its ideal low value of direct band gap of 1.5 eV at RT. Though CdTe thin films present high resistivity of the order of 10^4 Ω·cm, surface electrical improvement may be achieved through thermal treatments (TT) under quasi-controlled $CdCl_2$ atmospheres. These post-deposition chlorine treatments have two well-known issues: contamination due to the residues of gaseous Cd and lack of reproducibility of the CdTe surface activation.

S. Jiménez *et alii* have determined the variations of structural, optical and electrical properties of amorphous and polycrystalline thin films of the semiconducting quaternary $Cu_x(CdTe)_yO_z$ [3]. They prepared thin films by reactive RF cosputtering at 200 °C from powder-pressed CdTe and metallic Cu targets, under different O_2 partial pressures and final

work pressures of 4.7 mTorr using argon (Ar). Pollycristalline and amorphous films were found under O_2 partial pressures of the order of $x10^{-4}$ and $x10^{-5}$ Torr, respectively. A general trend of reduction of the lattice parameters of both cubic and hexagonal structures of CdTe was measured through X-ray diffraction measurements. Raman spectroscopy revealed a widening of the LO phonon mode peak upon the increment of Cu and O incorporation. The absorption edges presented shifts to lower energies upon Cu incorporation and shifts to higher energies as a function of the O_2 introduction. Band gap values varied from 2.3 to 09 eV in the amorphous samples, while those of the polycrystalline samples were maintained around 1.5 eV. Hall effect and 4-point probe method measurements showed hole concentration and mobility values of $3.3x10^{17}$ cm^{-3} and 11.3 $cm^2 \cdot (Vs)^{-1}$, respectively. The measured resistivity values were found in a wide range between $\sim 10^5$ and ~ 1 Ω·cm.

G. Arreola *et al.* showed the modifications of the structural and optical properties of the CdTe host in thin films upon the doping amounts of CuO in CdTe powder-pressed targets [4]. For RF sputtering depositions employing $(CdTe)_x(CuO)_y$ powder-pressed targets, the expression of the CuO nominal concentration in the dielectric targets is shown in Eq. (3.1).

$$\frac{\#\text{CuO molecules}}{\#\text{CdTe molecules}} \cdot 100\,\% = \text{CuO at}\%, \qquad (3.1)$$

Inverse tendencies of the Cd and Cu elemental concentrations were found through energy dispersive spectroscopy (EDS) chemical analysis of the CdTe + CuO (CCTO) thin films fabricated at different substrate temperatures (T_S). X-ray diffraction (XRD) and transmission electron microscopy (TEM) measurements reveald different preferred orientations of the cubic and hexagonal phases of CdTe. Through optical spectroscopies were detected shifts in the band gap energies for the deposited thin films, so as in the critical points of the cubic phase of CdTe. Band gap values varied between x and y. Critical points energies varied around. It was found for high concentrations of CuO the combination of semiconducting material CdTe and the metallic material $Cu_{2-x}Te$.

The fabrication of CCTO thin films at RT exposed in this work is based on the latter reports with the intention of employing the quaternary as the absorber layer in thin-film solar cells.

The electronic band structure of the cubic CdTe phase is shown in Figure 3.9. The band gap value E_g is illustrated at the Γ point and the critical points E_1 and $E_1+\Delta_1$ are shown in the Γ-L direction within the reduced band scheme in *k*-space.

Figure 3.9. Zincblende CdTe electronic band structure [5].

3.4. Zinc oxide.

ZnO is member of the II-VI family of semiconducting compounds. Due to the relatively large difference between the values of electronegativity of both species ($\chi_{Zn}=1.59$, $\chi_O=3.61$, in the Allen scale), its chemical bonding is predominantly ionic. Figure 3.10 shows the ZnO polytypes. ZnO crystals are found in nature with hexagonal and cubic arrangements. Figure 3.10(a) shows the hexagonal zincite structure. Figure 3.10(b) depicts the cubic zincblende phase of ZnO. The rocksalt structure of Figure 3.10(c) can be found under high hydrostatic pressures. The zincite phase is the most common arrangement of Zno crystals found in nature or fabricated in laboratories, due to its greater stability over the other two polytypes. Common lattice parameters of the zincite structure are $a=b=3.25$ Å and $c=5.20$ Å.

This semiconducting compound has been used as a transparent conducting oxide due to its relative low value of resistivity as deposited at room temperature (RT). Common resistivity values of ZnO thin films fabricated without intentional

heating programs are of the order of 10^{-1} Ω·cm. ZnO thin films are optically transparent to visible light, hence, it possess a high value of band gap, commonly reported as 3.37 eV at RT.

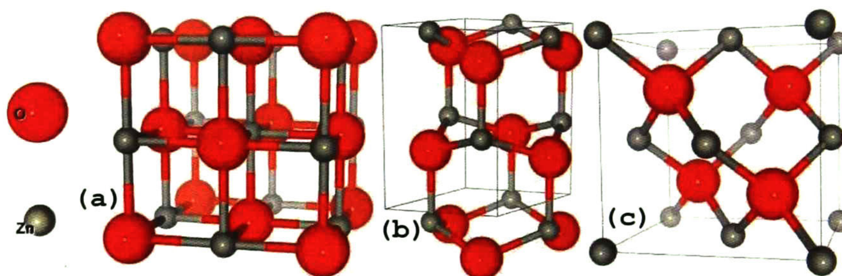

Figure. 3.10. ZnO polytypes. (a) Rocksalt, (b) Zincite and (c) Zincblende structures.

A. Beristain [6] determined the structural, optical and electrical properties of both doped and undoped crystalline ZnO thin films. He prepared thin films fabricated by RF sputtering from RT to higher temperatures such as 450° C, with 100 W of RF power on glass substrates and silicon. He reported crystalline films with well-oriented crystallite sizes of 177 Å through X-ray diffraction measurements and MDI Jade analysis of the undoped samples fabricated at RT. Raman spectroscopy revealed the presence of E_2^{low}, E_2^{high} and A_1(LO) phonon modes at 101, 437 and 576 cm^{-1}, respectively. AFM measurements provided surface roughness of the order of 17 nm and surface particle sizes of 290 nm. By UV-Vis measurements an averaged 80% of transmittance and 15% of reflectance of the thin films were determined. Electrical measurements through Hall effect with Ag metallic contacts followed by Van der Pauw squared geometry were performed. Majority charge carrier concentration, mobility, conductivity and resistivity values were obtained as 3.29×10^{19} cm^{-3}, 54.4 $cm^2 \cdot V^{-1} s^{-1}$, 3.05×10^2 $\Omega^{-1} \cdot cm^{-1}$ and 3.27×10^{-3} Ω·cm, respectively, for the undoped samples fabricated at RT.

The fabrication of ZnO thin films at RT exposed in this work is entirely based on the latter report with the intention to use this transparent semiconductor as the window layer of thin-film solar cells.

The electronic band structure of the zincite phase is shown in Figure 3.11. The band gap value of ~3.37 eV is illustrated at the center of the reduced scheme of energy bands of the hexagonal structure of ZnO, i.e. the Γ point.

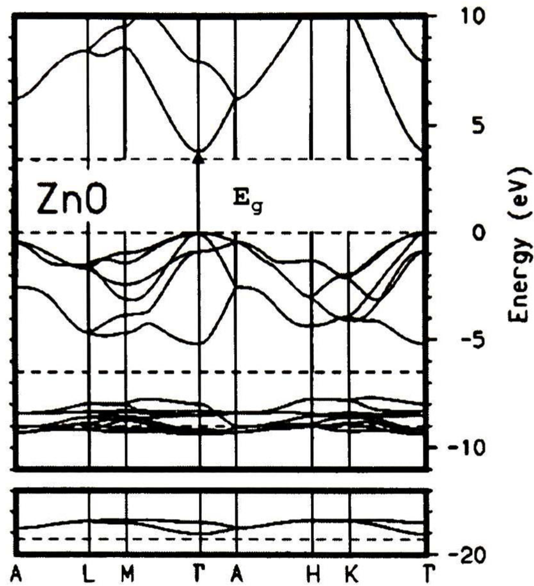

Figure 3.11. Zincite ZnO electronic band structure [7].

References.

[1] Solar spectrum calculator. Retrieved June 24, 2015 from https://pvlighthouse.com.au/calculators/solar%20spectrum%20calculator/solar%20spectrum%20calculator.aspx.

[2] Best research cell efficiencies. Retrieved September 03, 2015 from http://www.nrel.gov/ncpv/images/efficiency_chart.jpg

[3] S. Jiménez-Sandoval, G. E. Garnett-Ruiz, J. Santos-Cruz, O. Jiménez-Sandoval, G. Torres-Delgado, R. Castanedo-Pérez, and E. Morales-Sánchez, J. Appl. Phys. **100**, 113713 (2006).

[4] A. Mendoza-Galván, G. Arreola-Jardóna, L.H. Karlssonc, P.O.Å. Perssonc, S. Jiménez-Sandoval, Thin Solid Films **571**, 3 (2014).

[5] D. J. Chadi, J. P. Walter, M. L. Cohen, Y. Petroff and M. Balkanski, Phys. Rev. B **5**, 8 (1972).

[6] A. Beristain-Bautista, M. Sc. Thesis(2011).

[7] D. Vogel, P. Krüger, and J. Pollmann, Phys. Rev. B **54**, 8 (1996).

4. Fabrication and characterization details.

4.1. RF magnetron sputtering.

The sputter deposition of thin-film coatings is a widely used fabrication process for bulk and nano devices. This physical vapor deposition (PVD) technique is widely employed in semiconductor-related industrial and academic laboratories. Controlled single-layer and high-quality depositions are obtained, in comparison with other chemical or physical coating techniques (chemical vapor deposition, dip/spin coating, sublimation/evaporation). It also holds low-cost operation, with respect to more energetic processes (atomic layer deposition, pulsed laser deposition). Metallic, ceramic, semiconducting and organic coatings can be effectively deposited by radiofrequency (RF) sputtering. A cross-sectional scheme of the RF magnetron sputtering system employed in this work is shown in Figure 4.1. Important components of the sputtering system are listed in Table 4.1.

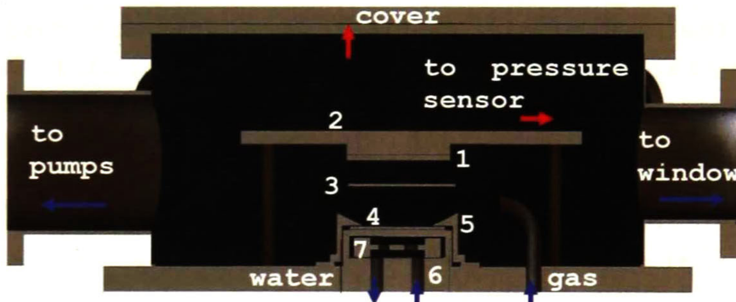

Figure 4.1. Sputtering system scheme.

Table 4.1. Components.

#	Item
1	Substrate
2	Sample holder
3	Shutter
4	Target
5	Gun cover
6	Sputter gun
7	Magnetron

The system is sealed by copper gaskets, vitton O-rings and vacuum grease. The atmospheric pressure reading according to the Oerlikon ITR90 gauge (wide range) is 7.50×10^2 Torr (10^{14} molecules/cm^3 [1]). A medium vacuum (10^{-2} Torr) is achieved by means of the Agilent DS102 mechanical pump, and the high

vacuum in the mid 10^{-5} Torr (10^{11} molecules/cm^3) is obtained with the Agilent V60 turbomolecular pump. Argon (Ar, inert gas) is introduced to the chamber, and the RF electric discharge starts the ionization of the gas atoms, i.e., it generates plasma. The positively charged particles are accelerated toward the cathode producing the erosion of the target material.

The substrate to be coated is fixed on a graphite holder, altogether mounted on a height-adjustable base. The target material is located below the substrate. A mechanical shutter is set between the substrate and target, with the intention to carry out pre-deposition sputtering. This procedure aids in dehumidification of the target, and prevents the deposition of non-intended material accumulated in the target´s surface during fabrication, storage and transportation.

The target material is located on the gun of the system, and has the shape of a disc, with 1/8″ in thickness and 2″ in diameter. The gun cover protects the sputtering gun from eroding. The former is connected to the chamber, and the latter is isolated from the chassis by rigid Teflon. The sputtering gun (cathode) and the chassis (anode) receive the RF power. The AC electric discharge amplitude oscillates between the gun and the chamber, and prevents a dielectric target to be charged during the erosion. An external impedance tuner is utilized to optimize the coupling of the RF power supply to the sputtering gun.

A magnetron is fixed beneath the target, within the sputtering gun. This magnetron generates an electron drift (managed by Lorentz force), describing a circumference parallel to the target´s surface. This effect increases the erosion rate, in comparison to a regular diode sputtering system [2]. Cold water supply maintains the magnetron in a functional temperature, preventing magnet damage at higher temperatures. Figure 4.2 exhibits the RF magnetron sputtering system utilized for the fabrication of the heterojunction solar cells. A pink Ar plasma can be observed in the vicinity of the target. Judicious election of material, welding and sealing is determinant to achieve non-contaminated depositions under high-vacuum conditions. Internal accessories must accomplish impeccable chemical and physical conducts as well.

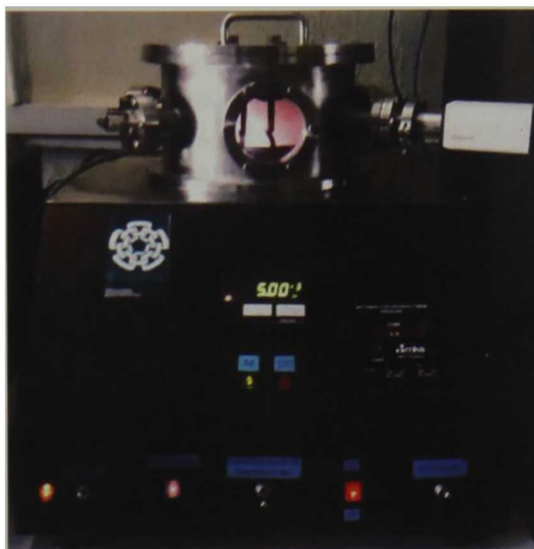

Figure 4.2. Franky sputtering system.

4.2. Topography and morphology.

Qualitative and quantitative information concerning the physical characteristics of the deposited material is a major topic in thin films fabrication. Properties such as thickness, surface roughness and grain size, can be obtained through several contact and non-contact techniques.

4.2.1. Mechanical profilometry.

Sloan Dektak II mechanical profilometer employs a stylus scan along a straight path to provide an X-Z profile of the sample. This 1-D plot depicts the height difference between the substrate and the deposited thin film, as a function of the path´s length. Figure 4.3 exhibits the tip scanning a thin film edge.

Figure 4.3. Stylus profilometry.

4.2.2. Optical profilometry.

Bruker Contour GT-K optical profilometer provides X-Z, X-Y and X-Y-Z profiles, based on light interference lines covering both substrate and thin film. Sharp interference fringes on the sample are monitored by a video camera. The distortion of these lines, caused by height difference, is recognized and the step size can be resolved. Figure 4.4 shows the white light spot on the sample´s edge, required for the thin film thickness characterization.

Figure 4.4. Optical interferometry.

4.2.3. Electron microscopy.

Philips XL-30 Environmental Scanning Electron Microscope (ESEM) and the Jeol JXA-8530F Electron Probe Micro Analyzer (EPMA) can provide high-resolution micrographs of a sample´s surface.

These equipments are able to produce an electron beam (e-beam), by heating a Tungsten (W) filament (in vacuum conditions), which are then accelerated toward a set of scanning coils. Independent electrical circuits are employed for the generation (medium voltage) and the acceleration (high voltage) of the e-beam. The scanning coils are responsible for the raster pattern (programed path) of the e-beam, on the sample´s surface. A couple of coils re-direct the e-beam in a straight line on the X direction of the sample. When the beam completes the X scan, the coils return to their original position; i.e. the e-beam returns to its starting point. Then, the Y coils allocate the beam just below the starting point, on the Y direction. The X coils are now able to perform the X raster pattern again. This process is carried out until the desired area is fully scanned [3].

When the e-beam strikes a solid at normal incidence, distinct signals are emitted from the sample´s surface. These signals consist of secondary and Auger electrons (electrons removed from the solid), retrodispersed electrons (electrons perpendicularly reflected), and X-ray and lesser energetic photons (radiative emission from de-excitation of atoms and heating of the sample material). Both ESEM and EPMA micrographs are based in secondary and retrodispersed electrons measurements. Surface characteristics in gray scale with micrometric resolution are provided through electron detectors and a specific analysis package. Transversal cuts of the deposited thin films aid in thickness measurements.

X-ray measurements through semiconducting detectors provide elemental composition analysis of the sample´s surface. Intense X-ray emissions by the surface, which are particular for each chemical element, are analyzed through energy dispersive spectroscopy (EDS) and the elemental composition (in units of mass or atomic concentration) is resolved. Figure 4.5 shows the grounded sample holder of the EPMA system. There can be observed Silver (Ag) paste on the samples. This is placed to avoid the semiconducting samples to be negatively charged, which tends to block the incoming e-beam.

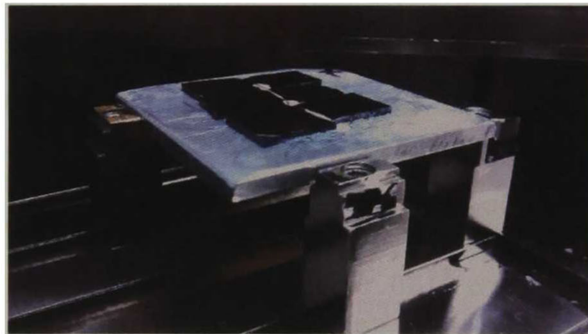

Figure 4.5. EPMA sample holder.

4.2.4. Atomic force microscopy.

Bruker Dimension 3100 Atomic Force Microscope (AFM) can resolve surface details with nanometric resolution. This system possesses a metallic tip that performs a fine raster pattern on the surface of a solid sample. The tip is attached to piezoelectric transductors, which permit the tip´s contraction or extension, according to the surface characteristics [3]. The acquired data consist of X-Y and X-Y-

Z plots. Average surface roughness and surface features sizes can be obtained from the graphs, through specific packages for image analysis. Figure 4.6 depicts an electrical measurement performed through an AFM system (Kelvin Probe Force Microscopy), with distinct hardware and software configuration but same mechanical procedure.

Figure 4.6. KPFM measurement.

4.3. Structural properties.

Atomic or molecular arrangement at the surface and bulk of a thin film has an inherent relation with the fabrication conditions. Distinct experiments permit the identification of the atomic environment through diffraction of ionizing radiation and dispersion of visible radiation (through interaction of light with static and dynamic dispersive centers present within the sample, respectively).

4.3.1. X-ray diffraction.

X-rays were first documented in 1895 by W. C. Roentgen. They consist of an ionizing radiation, with wavelengths within the range of 1.0×10^{-5} to 100.0 Å (1 Å = 1×10^{-10} m). Usual X-rays production is based on deceleration of high-energy electrons, through collisions with solid metallic targets. This process generates a wide band of X-rays wavelengths. The photon energy (E_γ) must equal the difference of the electron kinetic energy (E_K), i.e. before and after the collision. This is expressed in Eq. 4.1.

$$E_\gamma = \frac{\hbar^2}{2m_o}(k_i^2 - k_f^2), \quad (4.1)$$

where k_i and k_f are the electron wave vector magnitudes before and after a given collision (such that $E_K^i > E_K^f$), $\hbar$ is the

Dirac's constant (Planck's constant h divided by 2π) and m_o is the free electron mass (9.10×10^{-31} kg). The value E_K^i is established by the acceleration potential, as observed in Eq. (4.2).

$$E_K^i = Ve, \qquad (4.2)$$

where V is the acceleration potential (commonly of the order of 10 kV) and e is the electronic charge (1.60×10^{-19} C). The value E_K^f, on the other hand, depends on the degree of deceleration of the electron after a given colliding event [3]. Sharp peaks of X-rays with high intensities are obtained through de-excitation of metallic ions in the target material. When an inner core electron (independent of chemical bonding) is removed by a collision with an accelerated electron, a hole is created. This process allows an electron of an upper quantum level to occupy the empty state (permitted by the selection rules for emission), by the creation of an X-ray photon. The photon energy will now be established by the difference in energy of the quantum states involved in the radiative transition, as expressed in Eq. (4.3).

$$E_\gamma^n = E_n - E_0, \qquad (4.3)$$

where E_0 is the constant energy of the lower (available) quantum state and E_n ($n = 1,2,..$) is the energy of an upper (occupied) state involved in the allowed transition. When the acceleration potential of Eq. (4.2) is such that an inner-core electron from the energetic state E_0 is removed, monochromatic radiation with energy E_γ^n is produced. The most intense emissions (most probable radiative transitions) consist of $k_{\alpha 1}$ and $k_{\alpha 2}$ emissions. Less probable k_β emissions are also encountered in X-ray diffraction measurements, with very low intensities.

Incident k_α X-rays onto a crystalline sample surface are dispersed by the first atomic layers of the material. Crystalline solids (typical internuclear distances of ~1 Å), generate destructive and constructive interference patterns of the dispersed radiation, as reported by M. von Laue in 1912. That same year, W. L. Bragg proposed a geometric approach to X-ray diffraction, by the means of optical interference due to the interaction of coherent light and regularly ordered matter in a rigid structure. Figure 4.7 illustrates the phenomenon of

reflection and consequent diffraction of X-rays wave vector k (geometrical optics). There can be observed distinct Bragg reflections, due to the interaction between X-ray photon waves and the electronic orbitals surrounding the atoms in positions X, Y and Z.

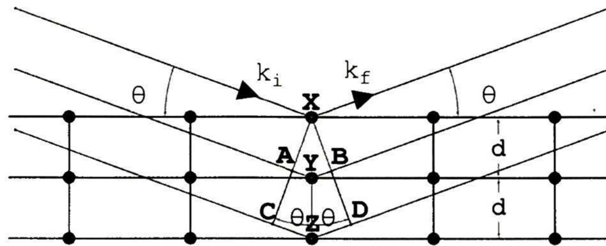

Figure 4.7. Bragg reflection.

Constructive and destructive interference imply an important geometrical condition for the reflected coherent rays. The optical paths $\overline{AY}$ and $\overline{YB}$ must succeed in a first condition embodied as $\overline{AY}+\overline{YB}=n\lambda$, where *n*, the diffraction order, is an integral number and λ is the X-ray wavelength. When this condition is accomplished, the dispersed radiation is in phase at the wavefront $\overline{XBD}$, and its coherence permits destructive and constructive interaction (their intensities add or substract, creating peaks or dips for the reflected radiation). A second condition arises when the angle of incidence θ is transferred within the $\overline{XAY}$ and $\overline{XBY}$ triangles (or $\overline{XCZ}$ and $\overline{XDZ}$ triangles). By trigonometry, the relation $\overline{AY}=\overline{YB}=d\sin\theta$ (or $\overline{CZ}=\overline{ZD}=d\sin\theta$) is found. These conditions are reduced to Eq. (4.4).

$$n\lambda = 2d_{hkl}\sin\theta, \qquad (4.4)$$

where d_{hkl} is the interplanar spacing between consecutive planes that belong to a given group of planes (*hkl*) (perpendicular to the direction [*hkl*]). The Miller indices *h*, *k* and *l*, are crystallographic points that describe a given (*hkl*) plane or group of planes of the crystalline environment, and are related to the orthogonal unit cell parameters *a*, *b* and *c* through Eq. (4.5).

$$d_{hkl} = \frac{1}{\sqrt{\left(\frac{h}{a}\right)^2+\left(\frac{k}{b}\right)^2+\left(\frac{l}{c}\right)^2}}, \qquad (4.5)$$

Specific packages for data analysis can be employed to analyze the measured diffraction pattern. Several values can be resolved, such as the interplanar spacings d_{hkl}, unit cell parameters *a*, *b* and *c*, and crystallite sizes (compound of unit cells oriented in a given direction [*hkl*] that construct the intense diffraction peaks measured by the system).

A Si wafer is employed as the reference material for the instrumental calibration of the JADE 6.5 package for diffraction pattern processing utilized in this work. Figure 4.8 shows the measured diffraction pattern, which corresponds to a Si cubic structure with preferred orientations on the [111], [220] and [311] directions (and their respective k_β). The PDF 27-1402 of the powder reference pattern is also shown.

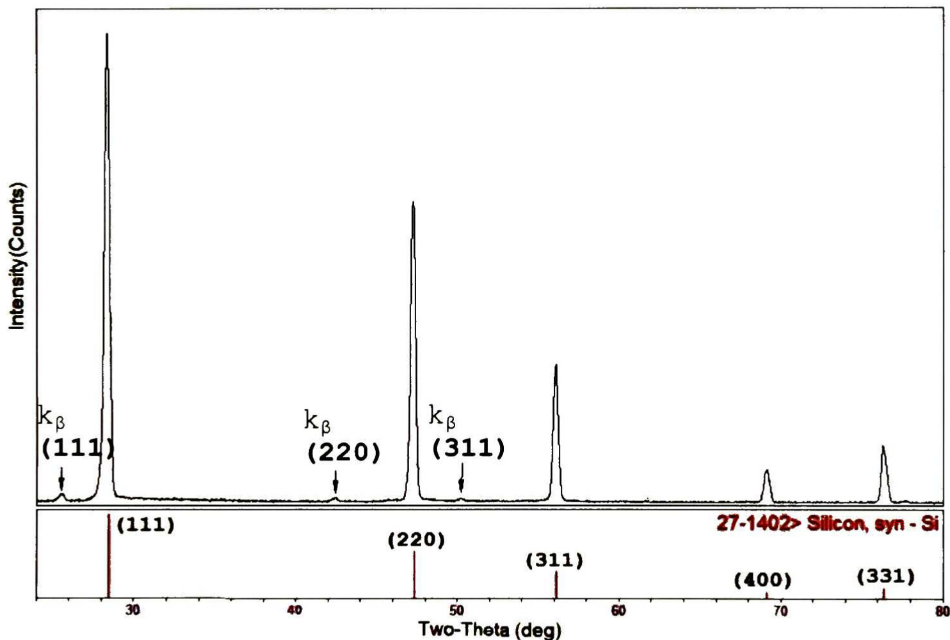

Figure 4.8. Calibration diffraction pattern of Si.

The Rigaku Dmax 2100 system is a powder diffractometer which employs a thin-film attachment to aid in the characterization of coated substrates, as shown in Figure 4.9. An alternating current (AC) electric discharge to a W filament generates the e-beam, which is directed to a Cu target ($k_{\alpha1} = 1.54056$ Å, $k_{\alpha2} = 1.54439$ Å, k_β = 1.39222 Å), responsible of the X-ray emission. A goniometer leads the detector through a circular path, and the diffraction is measured through parallel beam geometry as a function of the 2θ path of the goniometer.

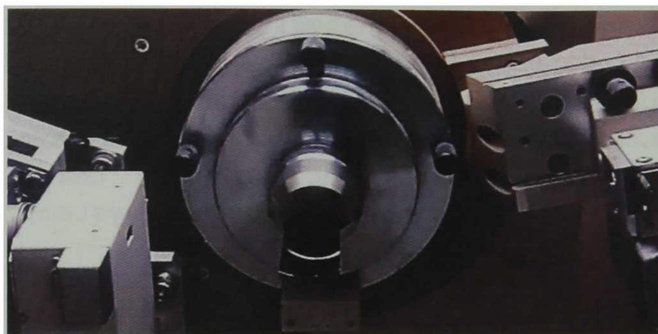

Figure 4.9. X-ray diffraction measurement.

4.3.2. Raman scattering.

Elastic scattering of light as the result of light-matter interaction was discovered by J. W. Strutt (Lord Rayleigh) in 1871. He proposed the dispersion of light waves by individual atoms or molecules smaller than the wavelength of the incident light. Elastically scattered photons are not differentiable, in terms of energy, from the incident photons. This implies that the Rayleigh dispersion consists of a parametric process, based on the re-emission of photons without a net exchange of energy between the light wave and the matter entity. Inelastically scattered photons, on the other hand, possess shifts in energy after the non-parametric interaction.

Inelastic scattering of light was predicted by A. Smekal in 1923, and was experimentally studied by C. V. Raman in 1927. He shined solar light through distinct substances and documented the observed light´s discrete shifts in energy after the interactions took place. This effect is due to light interaction with the vibrational modes of molecules in the corresponding substances (such as N_2 and O_2 molecules in air, or H_2O in water). Two inelastic processes come to place at normal temperature conditions: annihilation of existing vibrational modes (less likely) and creation of vibrational modes (more likely).

Crystalline vibrational modes arise from modeling a 1-D chain of atoms in a non-rigid structure as mass-spring systems composed by the nuclei and molecular orbitals. Electrically charged or neutral nuclei in the crystalline structure oscillate constantly around their equilibrium positions. Molecular orbitals act as the restoring forces that contribute to the expansion and contraction of the chains. This motion

propagates as a discrete package of energy named *phonon* throughout the crystal lattice. These entities possess natural frequencies of oscillation within the range 10^{12}-10^{13} Hz, associated to photon energies within the infrared (IR) band [4]. As with electrons, phonon modes are also distributed in bands: optical (higher energy) and acoustical (lesser energy) bands. Two categories of phonon modes arise by the relative motion of the atoms in regard to the phonon wave vector, namely longitudinal and transversal phonon modes. In the latter, the oscillations are perpendicular to the phonon wave vector, and in the former the oscillations are collinear with the propagation path. Figure 4.10 depicts photon wave vectors before and after interactions with the dynamic lattice.

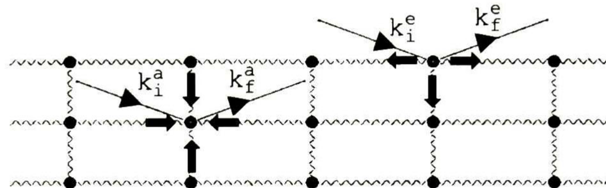

Figure 4.10. Phonon absorption and emission.

When a visible laser is shined on a crystalline sample´s surface, most of it is reflected, leading to the zero-order or Rayleigh reflection (most intense signal in Raman scattering characterization). A few portion of the dense light wavepacket exchanges energy with the molecular orbitals within the crystal. This leads to constant generation of e^--h^+ pairs that perturb the crystalline environment within the spot of incidence. This collective excitation is able to interact with the lattice, by means of emission or absorption of phonons. Through recombination of a photogenerated e^--h^+ pair, which has lost or gained energy, a photon is emitted. The photon energy will possess a discrete shift of energy, depending on the energy $\hbar\Omega$ of the involved phonon, as expressed in Eq. (4.6).

$$\hbar\omega_f = \hbar\omega_i \pm \hbar\Omega , \tag{4.6}$$

where Ω is the natural frequency of the phonon (in radian/s) and the $\pm$ signs correspond to absorption or emission of a phonon, respectively. These processes are named anti-Stokes and Stokes shifts, respectively. The latter is the event considered for Raman scattering measurements. The intensity of this process is much less than the Rayleigh reflection. Components of a Raman scattering measurement equipment consist

of a monochromatic light source, optical lenses and a sensitive radiation detector, capable of detecting the low intensity Stokes signal. Figure 4.11 shows the Raman spectrum of the Si wafer employed for the instrumental error calibration. Transversal-optical (TO) and the doublet of the transversal-acoustical phonon modes of the Si-Si covalent chains are responsible of the 300 and 520 cm^{-1} shifts.

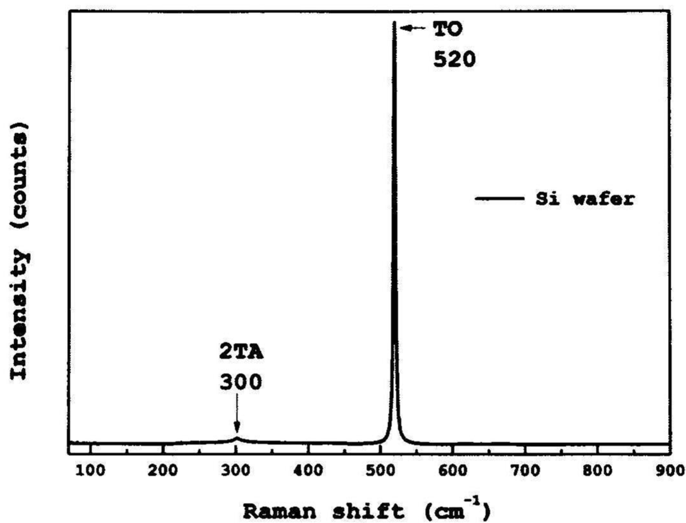

Figure 4.11. Reference Si Raman spectrum.

Dilor LabRAM II and Horiba LabRAM HR Evolution microscopes possess distinct laser sources and optical magnifications that allow non-destructive and focalized measurements of the dispersed photons. The accumulation of the dispersed light within the measurement time is reported as counts against Raman shift in wavenumber units (cm^{-1}). Figure 4.12 shows the Raman scattering characterization using the 632.8 nm He-Ne laser.

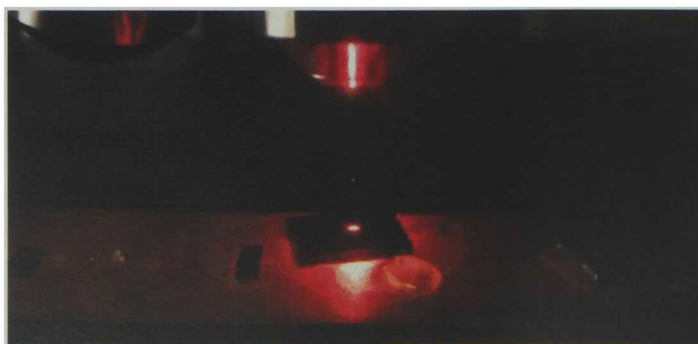

Figure 4.12. Raman scattering measurement.

4.4. Optical properties.

The optical behavior of a sample, in terms of reflection, transmission and absorption of light, is a major characteristic of thin-film PV devices. Optical parameters such as reflection and transmission coefficients (R and T), can be obtained through optical spectroscopies. Band gap magnitudes can be resolved from the transmission spectra through modeling of the absorption edge.

The process of light absorption may be modeled as a mass-spring system in which the electron is the dynamic mass and its attraction to the static positive nucleus acts as the restoring force. These atomic oscillators possess natural frequencies within the range of 10^{12}-10^{13} Hz, associated to ultraviolet, visible and near-infrared (UV-VIS-NIR) photons [4]. Figure 4.13 depicts a solid slab within a vacuum, with shining red, green, and blue (RGB) light at normal incidence.

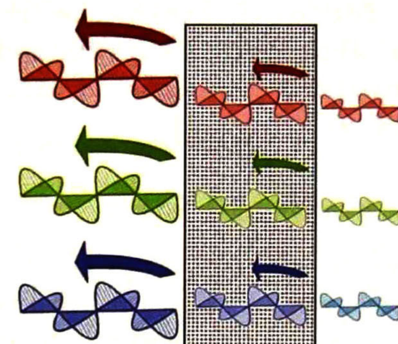

Figure 4.13. Light-matter interaction phenomena.

RGB light photons travel as EM waves in vacuum, until a different density of matter is reached. Light photons then propagate through the material experiencing dispersion by non-resonant polarization of atomic oscillators. If the solid is transparent, the amount of reflected and transmitted radiation must equal the incident intensity, i.e., $R+T=1$. For an opaque solid, resonant polarizations take place, and the EM waves exchange energy with the atomic oscillators, and the absorbed amount of light must contribute to the conservation of energy as $R+T+A=1$.

J. H. Lambert in 1760 and A. Beer in 1852, both stated that intensity of light waves propagating through a material diminished as a function of the thickness and concentration of

the sample, respectively. A general form of the Beer-Lambert law establishes the exponential attenuation of light´s intensity as a function of the thickness of the sample and its absorption coefficient α, as stated in Eq. (4.7).

$$I(z) = I_0 e^{-\alpha(\lambda) d} , \quad (4.7)$$

where I(z) is the instant intensity at a given point z within the solid, I_o is the incident intensity, $\alpha(\lambda)$ is the absorption coefficient at a given wavelength and *d* is the sample´s thickness. From this attenuation law, an expression for the absorption coefficient can be derived as Eq. (4.8).

$$\alpha(\lambda) = -\frac{\ln T}{d} , \quad (4.8)$$

where the transmission coefficient T is defined as the ratio of the instant intensity I(z) within the solid (or transmitted intensity I_T beyond the solid) to the incident intensity I_o. A detailed expression for $\alpha(\lambda)$ links the relative positions of the VB and CB edges with the electron and hole distributions within the bands involved in allowed direct transitions, as established in Eq. (4.9).

$$\alpha(\lambda) = A(hv - E_g)^{1/2}, \quad (4.9)$$

where hv is the photon energy, E_g is the band gap and the constant A is worked out from the probability for allowed direct transitions, namely the Fermi golden rule. A plot of the product $(\alpha(\lambda) hv)^2$ against photon energy *hv* sets a linear dispersion just after absorption is originated. Band gap values can be estimated from the extrapolation of this edge of absorption to the photon energy axis. This consideration is based on Eq. (4.9) for $\alpha(\lambda) = 0$ prior to absorption. This leads to a photon energy *hv* equal to the direct band gap E_g [4].

The FilmTek 3000 system (Scientific Computing Inc.) provides reflectance and transmittance measurements at same time and spot of incidence. A deuterium-halogen light source supplies visible light in the range of 240 nm (UV) to 840 nm (NIR). Figure 4.14 shows the spectroscopic characterization of the reference for light transmission, i.e. a glass substrate.

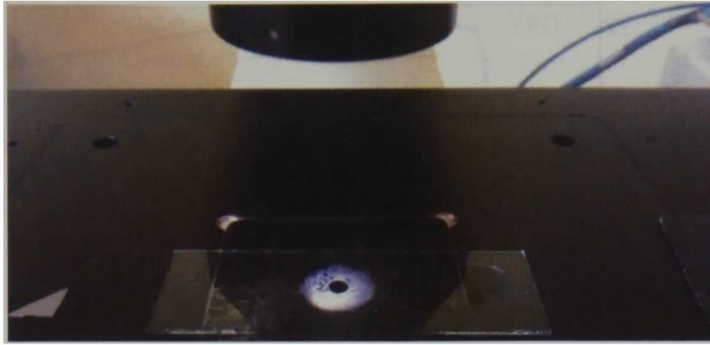

Figure 4.14. Glass substrate R and T measurement.

4.5. Electrical properties.

Knowledge of electrical parameters such as mobility, conductivity, type and concentration of majority charge carriers present in the semiconducting thin films support their adequate utilization in heterojunction-based devices. Distinct electrical measurements are based on thermal and magnetic perturbations. Electron work functions indicate electric behavior at junctions, and can be determined through surface potential microscopy.

4.5.1. Hot-point probe method.

The hot-point probe technique represents an effective, simple and quick method to determine the type of majority charge carriers present in a given extrinsic semiconducting sample. A standard arrangement for this characterization consists of a voltmeter and a heat source. The voltmeter probes are settled on the sample at RT and initial values for the surface potential difference are measured. Then, contact between the hot probe and the sample is performed within the vicinity of the positive tip. This establishes a temperature gradient between the hot point and the negative tip at RT.

Thermally excited majority charge carriers are able to diffuse into colder regions, leaving behind charged nuclei (positive and negative ions, for *n*-type and *p*-type samples, respectively). A positive step is consequence of electron diffusion onto the negative tip vicinity. A negative step is due to holes population increase within the negative tip region [5]. Actual potential difference profiles of Si reference wafers are shown in Figure 4.15.

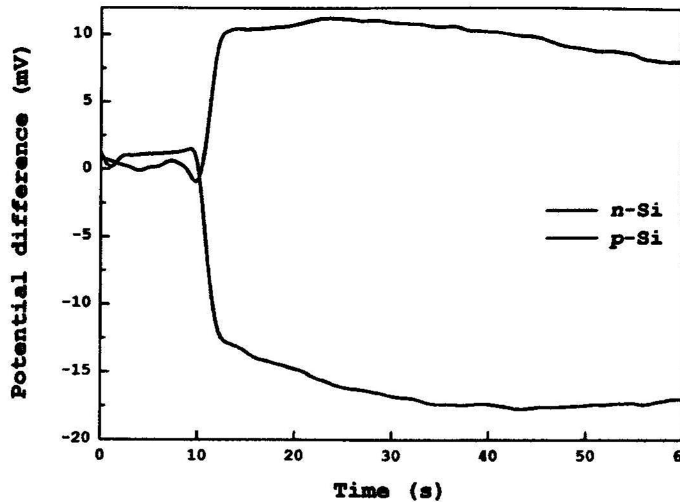

Figure 4.15. Reference Si wafers potential differences.

The hot-point probe system employed in this work is shown in Figure 4.16. The observed configuration allows the placement of the BK Precision 5492 Bench Multimeter probes on a thin film surface with ~1 cm spacing. The Weller WES51 Soldering Station acts as the temperature-controlled heat source. Through specific software, a profile of the measured potential difference between the probes against time is obtained.

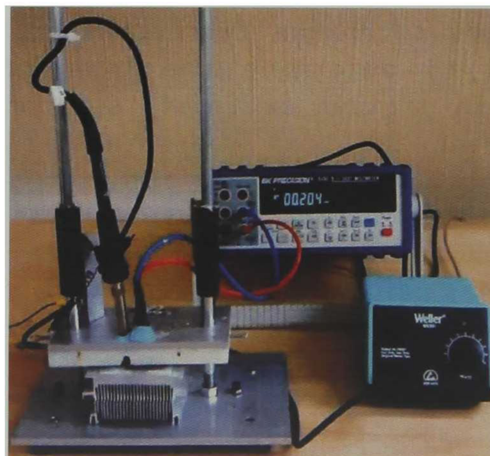

Figure 4.16. Hot-point probe system.

4.5.2. Hall effect.

The Hall effect consists in the generation of an electric field $\mathbf{E}_H$ due to a magnetically induced spatial separation of free charge carriers present in a sample, as observed by H. E. Hall in 1879. Figure 4.17 schematizes a Hall effect

measurement for thin films following Van der Pauw geometry with metallic contacts.

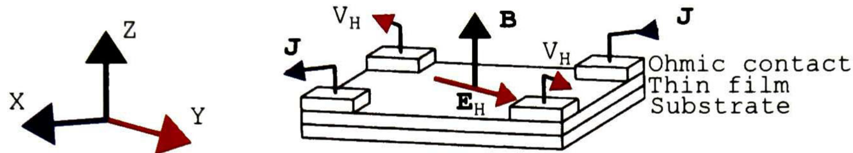

Figure 4.17. Hall effect geometry.

A current density **J** is supplied to opposite corners of the squared sample in X direction, in presence of a magnetic field **B** applied on the Z direction. The DC current experiences a deflection managed by the magnetic force expressed in Eq. (4.10).

$$F_B = (e\mathbf{v} \times \mathbf{B}), \qquad (4.10)$$

where **v** is the drift velocity of the charge carriers and e is the fundamental electronic charge. The cross product indicates that the current is deflected perpendicularly to the X-Z plane, i.e. into the Y direction. The accumulation of charge carriers induces an electrical field $\mathbf{E}_H$ that counterbalances the magnetic force (i.e. in -Y direction), leading to an equilibrium in which the deflection is interrupted. From this steady state situation, the Hall field relates to the magnetic force as expressed in Eq. (4.11).

$$\mathbf{E}_H = R_H(e\mathbf{v} \times \mathbf{B}), \qquad (4.11)$$

where the proportionality factor R_H is the Hall coefficient, and its measured sign indicates whether the majority charge carriers responsible of $\mathbf{E}_H$ are electrons or holes.

Applying classical mechanics to describe the behavior of a free charge carrier in presence of both electric and magnetic fields, Newtown´s second law takes the form of Eq. (4.12).

$$m^* \left(\frac{d\mathbf{v}}{dt} + \frac{\mathbf{v}}{\tau}\right) = -e\mathbf{E} - (e\mathbf{v} \times \mathbf{B}), \qquad (4.12)$$

where m^* is the particle´s effective mass, τ is the mean time between consecutive collisions with static or dynamic centers of dispersion, and $e\mathbf{E}$ and $e\mathbf{v} \times \mathbf{B}$ are the electric and magnetic forces experienced by the particle, respectively. This expression describes the acceleration of a particle that is

part of a current density $\mathbf{J}$ managed by an electric field $\mathbf{E}$ but perturbed by a magnetic field $\mathbf{B}$. It also takes into account the fact that particles may experience collisions with point defects, impurities, other particles or phonons present in the sample in thermodynamic equilibrium at RT [6]. The current density $\mathbf{J}$ is related to the drift velocity $\mathbf{v}$ through the population of particles per unit volume of the solid N and their electrical charge, as stated in Eq. (4.13).

$$\mathbf{J} = \mp Ne\mathbf{v}, \qquad (4.13)$$

where the $\mp$ signs stand for electrons and holes, respectively. The applied $\mathbf{E}$ supplies the driving force responsible of the drift velocity $\mathbf{v}$ of the current density $\mathbf{J}$ and can be related through the solution of Eq. (4.12).

A solution for the dynamical equation with no applied $\mathbf{B}$ and in steady state, in which the physical properties of the system do not change with time, is expressed in Eq. (4.14).

$$\mathbf{v} = -\frac{e\tau}{m^*}\mathbf{E}, \qquad (4.14)$$

where $e\tau/_{m^*}$ is defined as the mobility μ, which acts as the proportionality factor between the drift velocity of the charge carrier and the applied $\mathbf{E}$, and is stated in Eq. (4.15).

$$\mu = \pm\frac{e\tau}{m^*}, \qquad (4.15)$$

where the $\pm$ signs stand for electrons and holes, respectively. Substituting Eq. (4.14) into Eq. (4.13), an equivalent definition for the current density $\mathbf{J}$ is obtained, as expressed in Eq. (4.16).

$$\mathbf{J} = -\frac{Ne^2\tau}{m^*}\mathbf{E}, \qquad (4.16)$$

where the proportionality factor between $\mathbf{J}$ and $\mathbf{E}$ is defined as the conductivity σ, as stated in Eq. (4.17).

$$\sigma = \pm\frac{Ne^2\tau}{m^*}, \qquad (4.17)$$

where the ± signs stand for electrons and holes, respectively, and N may be substituted for the majority charge carriers concentrations n and p for electrons and holes, as well.

The Ecopia HMS-5000 system is a fully automated equipment which provides voltage measurements of ~1-square-cm thin films perpendicularly paired with a current supply, in presence of a 0.55 Tesla magnetic field. The gold-coated sample holder of the Hall effect measurement system with square 4-point probe configuration is shown in Figure 4.18.

Figure 4.18. Hall Effect characterization.

Figure 4.19 shows typical I-V linear relations for point-like metallic ohmic contacts on a semiconducting sample. This behavior allows for a correct measurement of the electrical mobility μ, conductivity σ, resistivity ρ ($^1/_\sigma$), type and concentration of majority charge carriers of an extrinsic semiconducting thin film.

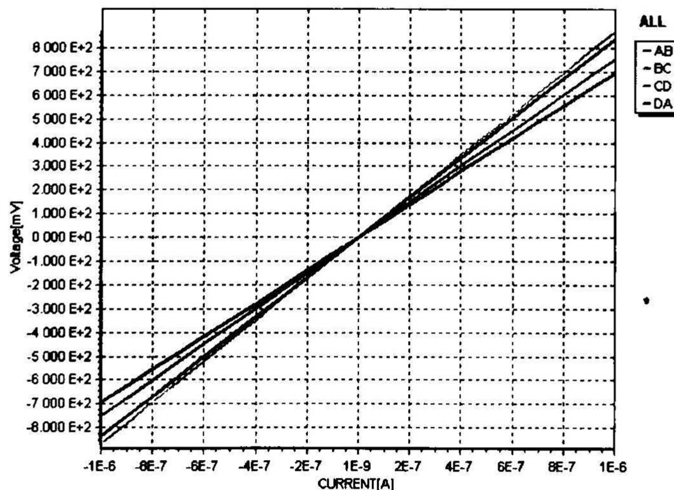

Figure 4.19. I-V curve by 4-point probe method.

4.5.3. Electron work function.

The electron work functions for semiconducting thin films can be obtained through Kelvin Probe Force Microscopy (KPFM). The electron work function is a surface property of a material, independent of its volume. It is defined as the energy of the last occupied state in a material in thermodynamic equilibrium at 0 K, measured with respect to the vacuum level. The photon energy $\hbar\omega$ capable of promoting an electron from the highest occupied state into the vacuum level must be the difference between the kinetic energy of a free electron and the surface work function of the material. This is stated in Eq. (1.1).

The vacuum level alignment for all the materials involved in a junction, before contact, is an important consideration for this surface characterization. It allows the interpretation for the band bending at the junction, with respect to the local vacuum level for each material.

Work function measurements can be carried out with the AFM system with KPFM configuration, as observed in Figure 4.6. The KPFM tip and the reference material, prior to contact, possess different Fermi levels with respect to the vacuum level (considered aligned for both). Through contact of both materials, the Fermi level is aligned, as consequence of electron diffusion from one material to the other. This process generates a deformation in the local vacuum levels at the junction [7].

Vacuum level deformation gives rise to opposite electrostatic charges for both materials, leading to electrostatic forces of attraction, once the materials are separated by a minimum distance. The equipment detects this attraction, and supplies a DC bias to the tip-reference system to counterbalance the electrostatic force. When the equilibrium is reached, the system records the amplitude of the supplied voltage. This voltage is named contact potential difference, and is related to the work functions of the materials through Eq. (4.18).

$$e\Delta V_{Au} = \Phi_{tip} - \Phi_{Au}, \tag{4.18}$$

where e is the electronic charge, ΔV_{Au} is the contact potential difference for the reference, Φ_{tip} is the work function of the KPFM tip, and Φ_{Au} is the work function of the gold (Au) thin

film reference. The latter is taken as constant for every measurement as $\Phi_{Au} = 5.1$ eV.

The configuration for the sample's measurement is equivalent to the reference measurement, as expressed in Eq. (4.19).

$$e\Delta V_S = \Phi_{tip} - \Phi_s, \tag{4.19}$$

Substituting Φ_{tip} from Eq. (4.19) into Eq. (4.18), the work functions for the semiconducting films are resolved.

Bruker Dimension 3100 AFM with KPFM configuration provides X-Y and X-Y-Z graphs of potential difference values as a function of the scanned area. Measurements are carried out in a sealed chamber with constant flow of dry air to provide a low-humidity atmosphere.

4.6. Band offset at junctions.

Electric transport between semiconducting and metallic materials is a prime subject in the fabrication of heterojunction-based devices. Most of the solid-state devices employ rectifying metallic contacts (non-linear I-V characteristics) to cease electrical conduction in applications involving high-speed switching. Solar cells, on the other hand, employ ohmic contacts (linear I-V characteristics) that are beneficial to constant and bidirectional flow of current.

Through flat band schemes, metal-metal, metal-semiconductor and *p-n* junctions can be predicted according to the properties of the involved materials with respect to the vacuum level, namely the crystal electron affinity and the electron work function. The crystal electron affinity (χ) is defined as the energy released by a solid, when an electron from the vacuum level is introduced to the bottom of the CB of the material. While the electron work function of an extrinsic semiconductor can be modified through doping, the electron affinity remains constant, independent of doping.

When two solids are submitted to contact with each other, matter exchange is carried out with the intention to balance the chemical potential in the two-body system. This involves that Fermi levels align through both materials and a

subsequent deformation for the local vacuum level arises at the junction.

The Schottky-Mott model applies for the band bending at the metal/semiconductor junction. This model predicts the generation of an electric field for majority charge carriers within the semiconductor and a Schottky barrier for electrons within the metal. The electric field, and hence, the potential barrier is generated within the semiconductor and avoids diffusion of majority charge carriers into the metal. This potential barrier is set by the bending of the band involved in the conduction of the extrinsic semiconductor, i.e. the VB maximum for *n*-type semiconductors or the CB minimum for *p*-type semiconductors. The Schottky barrier is generated within the metallic material and its magnitude is set by the difference in energy between the bent band and the Fermi energy.

Band alignment for a metal/*p*-semiconductor junction in which $\Phi_m > \chi_p$ is depicted in Figure 4.20. Electron waves and hole waves are schematized within the metal and *p*-semiconductor bands, respectively. Figure 4.20(a) depicts the bands prior to contact. Figure 4.20(b) shows both Schottky and built-in potential barrier created at the junction.

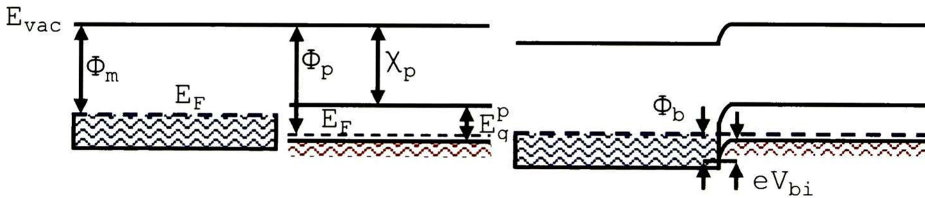

Figure 4.20. Metal/*p*-semiconductor junction. (a) Before and (b) after contact.

The Schottky and potential barrier created at the metal/*p*-semiconductor junction with $\Phi_m > \chi_p$ are expressed in Eq. (4.20) and Eq. (4.21) respectively.

$$\Phi_b = E_g^p + \chi_p - \Phi_m, \tag{4.20}$$

$$eV_{bi} = \Phi_m - \Phi_p, \tag{4.21}$$

A similar situation arises for the *n*-semiconductor/metal junction in which $\Phi_m > \chi_n$, as observed in Figure 4.21. Electron waves are schematized within the metal and *n*-semiconductor bands. Figure 4.21(a) depicts the situation for the materials

prior to contact. Figure 4.21(b) shows both Schottky barrier and the built-in potential created at the junction.

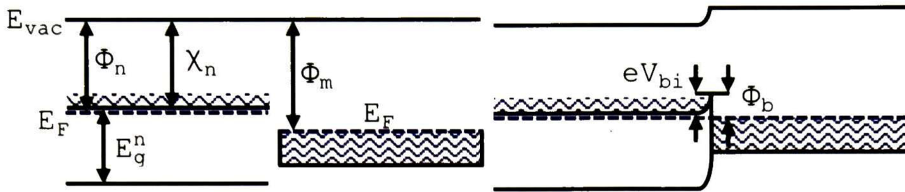

Figure 4.21. *n*-semiconductor/metal junction. (a) Before and (b) after contact.

The Schottky and potential barrier created at the *n*-semiconductor/metal junction with $\Phi_m > \chi_n$ are expressed in Eq. (4.22) and Eq. (4.23) respectively.

$$\Phi_b = \Phi_m - \chi_n, \tag{4.22}$$

$$eV_{bi} = \Phi_m - \Phi_n, \tag{4.23}$$

The opposite cases for the described metal/semiconductor junctions are ohmic contacts (no generation of Schottky barrier). In these, band deformations are beneficial to hole and electron flow from the semiconductors into the metallic contact and viceversa, such that $\Phi_m < \chi_n$ and $\Phi_m < \chi_p$.

Anderson model applies for the band offset at the *p-n* junction, based on the crystal electron affinities of the semiconductors. These values are independent of doping, and are considered as material´s constants. CB and VB edges suffer deformations at the *p-n* junction, and can be predicted through the Anderson´s rules, stated in Eqs. (4.24) and (4.25).

$$\Delta E_c = \chi_n - \chi_p, \tag{4.24}$$

$$\Delta E_v = (\chi_p + E_g^p) - (\chi_n + E_g^n), \tag{4.25}$$

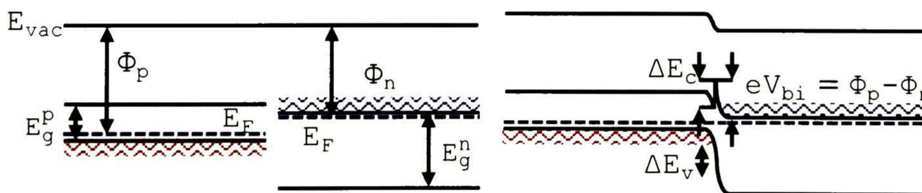

Figure 4.22. *p-n* heterojunction. (a) Before and (b) after contact.

4.7. Solar cell performance.

The equivalent electric circuit for a solar cell under illuminated conditions at RT is schematized in Figure 4.23.

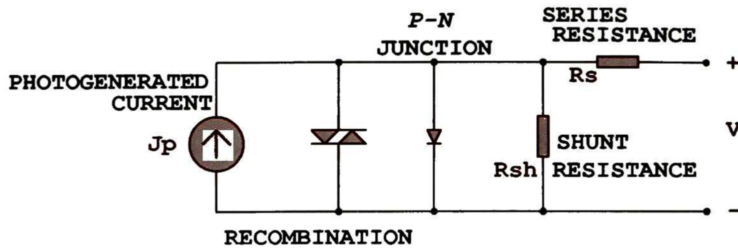

Figure 4.23. Illuminated solar cell electrical model [8].

As stated in Figure 3.6, the rectifying characteristics of the *p-n* junction are obtained under the application of a forward voltage between the terminals of the solar cell in dark conditions at RT. When the solar cell is illuminated, a supply of photogenerated current yields a displacement of the measured rectifying I-V curve. Current loss exists through the recombination of the photogenerated e^{-}-h^{+} pairs within the semiconductors. Three types of recombination mechanisms may exist within the device: (1) radiative recombination, in which the exciton (e^{-}-h^{+} pair) recombines through a CB-to-VB transition with an emission of a photon with energy $\approx E_g$, (2) Auger recombination, where the e^{-}-h^{+} pair recombines and gives away its energy to an e^{-} in the CB, and (3) Shockley-Read-Hall recombination, in which the promoted e^{-} is trapped by a defect level within the band gap of the semiconductor. This energy state may be deliberately introduced by doping or unintentionally by lattice defects generated during fabrication.

Parasitic resistances within the device also represent current loss and are often excluded of the electric circuit equivalent of a solar cell. The series resistance R_s and the shunt are present due to the junctions found in the solar cell, namely at the metal/semiconductor junctions. The shunt resistance (parallel) R_{sh} exists due to pin holes or short circuits generated during the fabrication of the device. Through Ohm´s relation $I=V/R$, low values for the series resistance R_s are ideal in order to get high values of current, while for the parallel resistance R_{sh} high values are expected, in order to

obtain high voltages between the terminals of the device. Common reported values of R_s are of the order of 10 $\Omega\cdot cm^2$ and of R_{sh} of the order of 1000 $\Omega\cdot cm^2$ for research solar cells.

The non-ideal equation for the I-V rectifying relation of a solar cell under illumination including loss due to parasitic resistances and recombination describes the displaced I-V curve shown in Figure 3.6. This is expressed in Eq. (4.26).

$$J = J_p - J_o \exp\left[\frac{e(V+IR_s)}{nkT}\right] - \frac{V+IR_s}{R_{sh}}, \tag{4.26}$$

where J is the current supplied by the device, J_p is the photogenerated current, J_o is the saturation current at which the potential barrier is surpassed by the majority charge carriers, k is the Boltzmann's constant, T is the absolute temperature, and n is the ideality factor, that accounts for the predominant recombination mechanism within the semiconductors.

The performance characterization is schematized in Figure 4.24, through a cross-sectional view of the PV device. Specific software is employed to deliver a DC bias in order to obtain the rectifying I-V relation for a *p-n* junction.

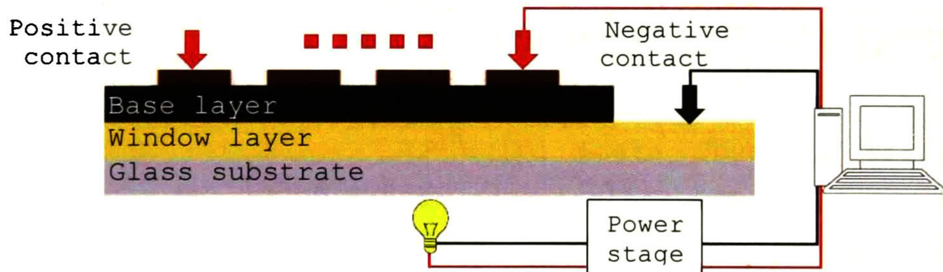

Figure 4.24. Solar cell performance measurement configuration.

Measured J-V and P-V relations of a 0.1 cm^2 polycrystalline Si solar cell are shown in Figure 4.25. Along with the J-V curve of the solar cell, the product J*V (power density P in mW/cm^2) is employed for η calculation.

The coordinates (V_{oc}, I_{sc}), (V_m, I_m) and (V_m, P_m) are indicated in the graph. V_{oc} is the open-circuit voltage and it is measured by a multimeter with an internal resistance with variable values lesser than 10^4 Ω/V. I_{sc} is the short-circuit current

and is measured with a resistance which does not allow a voltage drop of 20 mV across its terminals. Their product sets the idealized maximum power to be drawn from the device (black-dashed rectangle). From the maximum real power Pm delivered by the solar cell (red-dashed rectangle), the maximum values of voltage and current are known, i.e., V_m and I_m.

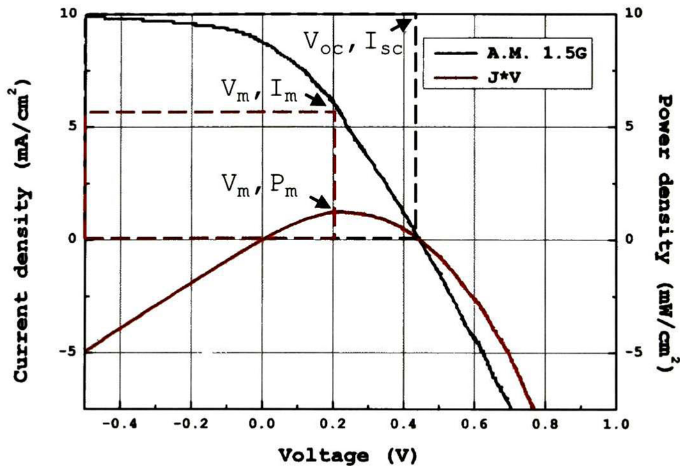

Figure 4.25. Si solar cell performance.

The efficiency value η is defined as the ratio of the output of the device (electrical power) to its input (radiative power) [9]. This is expressed in Eq. (4.23).

$$\eta = \frac{V_{oc} I_{sc} FF}{P_{in}}, \tag{4.23}$$

where P_{in} is the radiative power and FF is the fill factor. The value P_{in} (supplied by the system) is a constant and equal to 100 mW/cm^2. This value is ensured once the system is calibrated with a commercial Si solar cell used as a standard. The quality factor FF is obtained through Eq. (4.24).

$$FF = \frac{V_m I_m}{V_{oc} I_{sc}} 100\%, \tag{4.24}$$

A solar simulator for superstrate solar cells is employed for the I-V characterization in dark and under A.M. 1.5G illumination. Figure 4.26 shows the I-V measurement of a 0.25 cm^2 heterojunction solar cell (glass/Al/ZnO/CCTO15/Cu) under A.M. 1.5G illumination. A graphite probe acts as the positive contact and indium (In) is used as the negative contact.

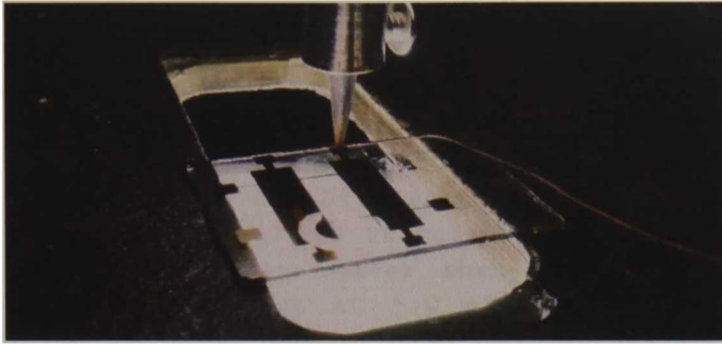

Figure 4.26. Efficiency measurement.

References.

[1] Roth, A. Vacuum Technology. Elsevier Science, Amsterdam (1996).

[2] Rossnagel S., Powell R., Ulman A. Thin Films, PVD for Microelectronics: Sputter Deposition Applied to Semiconductor Manufacturing. Academic Press, San Diego (1998).

[3] Skoog D., Holler F., Crouch S. Principles of Instrumental Analysis. Thomson Brooks/Cole, Belmont (2006).

[4] Fox M. Optical properties of solids. Oxford University Press, UK. (2010)

[5] A. Axelevitch, G. Golan. Electronics and Energetics **26**, 3 (2013).

[6] Hook, J.R., Hall, H. E. Solid State Physics. Wiley, England. (1991).

[7] S. Kalinin, A. Gruverman. Scanning Probe Microscopy **II**, Springer, USA (2007).

[8] A. Shah, P. Torres, R. Tscharner, N. Wyrsch, H. Keppner, Science **285**, 5428 (1999).

[9] Efficiency. Retrieved April 20, 2015 from http://pveducation.org/pvcdrom/solar-cell-operation/efficiency

5. Experimental details.

Every deposition was carried out in an RF magnetron sputtering system, on CORNING 2947 glass substrates. These glass substrates were subdued to a rigorous cleaning technique with chromic solution (at RT for 24 hours) and nitric acid (at high temperature for 3 hours). The target-substrate distance was 5 cm. The base pressure was lesser than $5.0\text{x}10^{-5}$ Torr and the work pressure was constant at 5.0 mTorr of Ar. The net RF power on the targets and sputter times varied for each material. The pre-deposition time was more than 5 min, with the shutter on. Clean stainless steel shadow masks were used for the fabrication of research-size solar cells and Van der Pauw metallic contacts.

5.1. CCTO thin films.

The sputtered CCTO targets were fabricated from 27 g of $(CdTe)_x(CuO)_y$ powder (CdTe: Aldrich, 99.99% pure; CuO: Electronic Space Products International, 99.999% pure), compressed by 20 tons for 30 min in a hydraulic press.

The net RF power on the dielectric targets was 40 W. The final deposition time varied for each target, as listed in table 5.1, along with the CCTO sample name.

Table 5.1. CCTO thin films deposition times.

CCTO	Time (min)	CCTO	Time (min)
0	120	10	132
2	122	11	133
3	123	12	134
5	126	13	135
6	127	14	136
7	128	15	138
8	129	20	144
9	130	25	150

5.2. Cu front contact.

The sputtered Cu target was a solid metallic disc (Kurt J. Lesker, 99.99% pure). The net RF power on the metallic target was 100 W, and the final deposition time was 2 min.

5.3. ZnO thin films.

The sputtered ZnO target was fabricated from 18 g of ZnO powder (Sigma-Aldrich, 99.99% pure), compressed by 12 tons for 10 min in a hydraulic press. The net RF power on the dielectric target was 100 W and the final deposition time was 17 min.

5.4. Ti/Al contact.

Two metallic targets were involved for the Van der Pauw contacts deposition (Kurt J. Lesker: Ti, 99.7% pure and Al, 99.99% pure). The net RF power on the metallic targets was 100 W, and the final deposition time was 25 min for Ti and 40 for Al.

6. Results and discussion.

Thickness values for the thin films and metallic contacts were obtained by means of mechanical and optical profilometry. Surface topography was acquired through AFM. Morphology and chemical analyses were performed through ESEM/EPMA measurements. Structural properties were resolved through X-ray diffraction and Raman scattering measurements. Electrical characterizations were carried out with the hot-point probe technique and Hall effect. UV-Vis spectroscopy was carried out to determine reflectance and transmittance characteristics. Band gap values were resolved by modeling direct transitions between parabolic bands. Electron work function measurements were performed with KPFM. The performance of the heterojunction solar cells was determined through efficiency measurements under A.M. 1.5G illumination.

6.1. CCTO thin films.

6.1.1. Topography.

The conditions described in section 5.1 result in thickness values of 2 µm at the substrate´s opposite ends for all depositions, and from 3 to 4 µm at the substrate´s center, from CCTO25 downward to CCTO0, respectively. Figure 6.1 shows the CCTO deposition on a glass substrate. Figure 6.1(a) shows the measured thickness distribution in a cross-sectional view. Figure 6.1(b) shows a planar view of the substrate-size deposition.

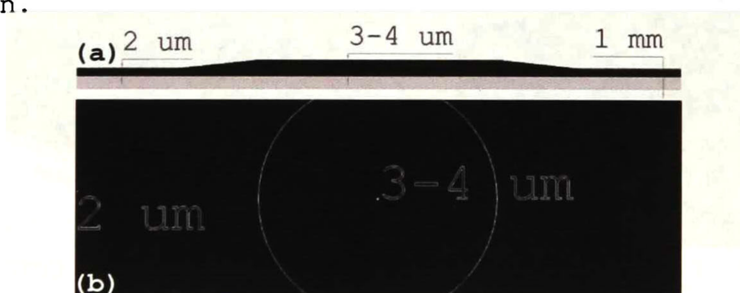

Figure 6.1. Base layer 3-D design. (a) Thickness and (b) distribution.

The reported difference in thickness between the substrate´s center and edges lies in the sputtering deposition nature and the erosion rates for the target materials. This effect was observed in all the depositions performed in this work, for both dielectric and metallic targets.

2-D and 3-D topographical maps acquired through KPFM measurements carried out in a 2.0% humidity atmosphere are shown in Figure 6.2. There can be observed structural features with distinct sizes and geometries from zero to higher nominal concentrations of CuO. Figure 6.2(a) shows pure CdTe spherical-like particles of 150 nm in diameter. Columnar-like structures with 150 nm in thickness and 600 nm in length are observed in Figure 6.2(b). Figure 6.2(c) shows features with diameter values lower than 100 nm.

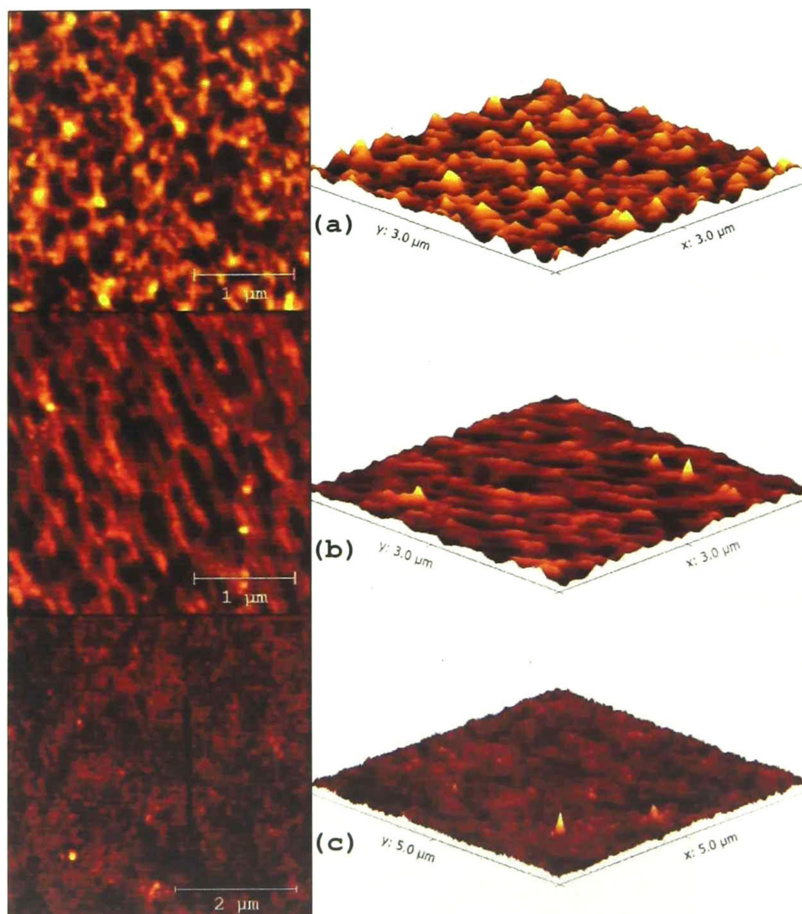

Figure 6.2. Topographical AFM images. (a) CCTO0, (b) CCTO10 and (c) CCTO25.

Analyses of these AFM images through Gwyddion 2.40 [1] reveal root means square (RMS) roughness values smaller than 4.30 nm for all the deposited CCTO thin films. Planar surface permits adequate adhesion of the subsequent layers for the PV device fabrication and of metallic contacts for electrical characterizations.

The observed behavior of surface particle sizes holds as well for the CCTO thin films not reported in this document. This effect allows for the conclusion that the incorporation of Cu and O in the host matrix (CdTe) tends to diminish particle sizes for the samples deposited at RT. This may be detrimental for the electrical behavior of the CCTO samples with higher CuO concentrations. Small sizes for surface features indicate small dimensions for the CCTO grains in the surface and bulk of the sample. Large number of grain boundaries represents larger probability of collisions by the majority charge carriers and is directly proportional to the mobility as measured through the 4-point probe method. Photogenerated e^{-}-h^{+} pairs may recombine after collision with grain boundaries.

6.1.2. Morphology.

Surface micrographies by ESEM/EMPA of the deposited thin films are shown in Figure 6.3, where a 250 µm squared uniform surface is observed. Structural features are also detected, following the tendency observed through AFM and Gwyddion.

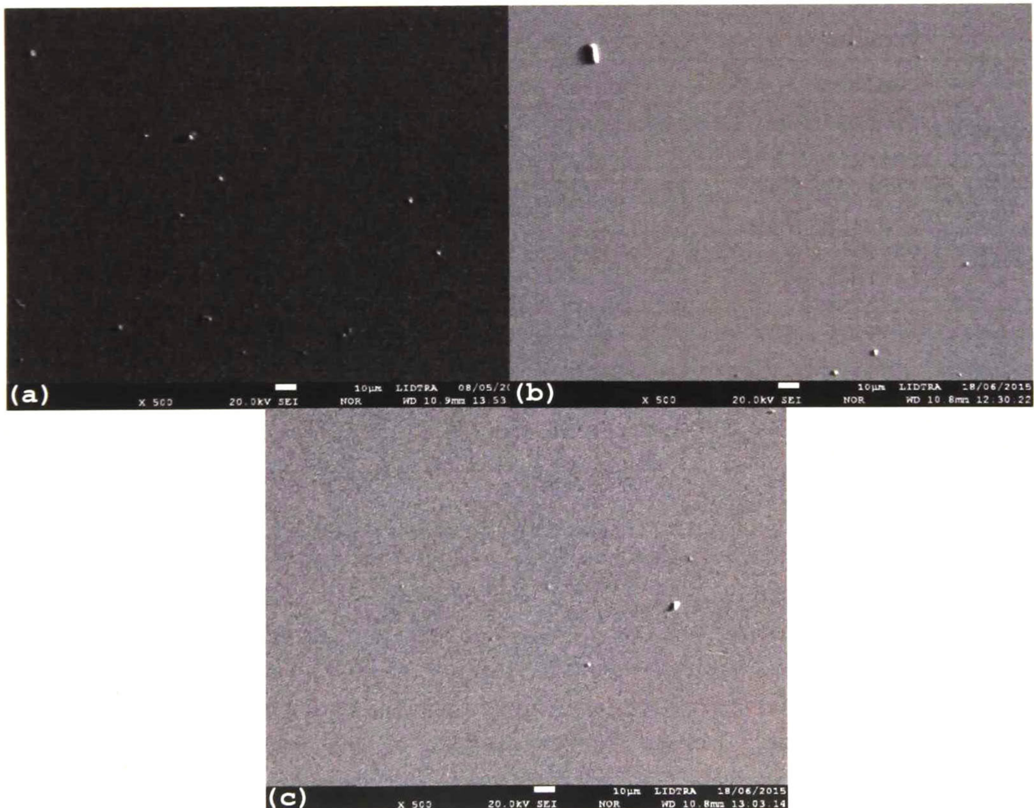

Figure 6.3. SEM images. (a) CCTO0, (b) CCTO10 and (c) CCTO25.

6.1.3. Chemical composition.

Figure 6.4 and Table 6.1 show the elemental compositions of the thicker regions (3-4 μm) of the CCTO samples. ESEM/EPMA measurement conditions consist in 20 kV and 0.10 nA of current for the e-beam and a 500x objective lens magnification.

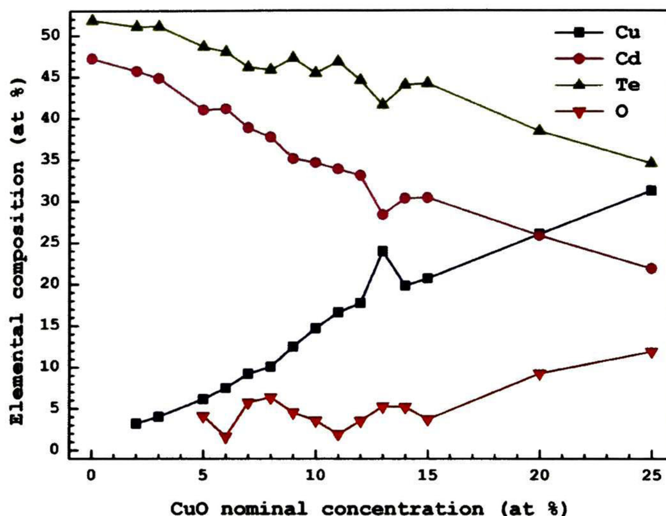

Figure 6.4. CCTO films elemental composition trends.

Table 6.1. CCTO films elemental composition results.

Sample	Elemental composition (at %)				Sample	Elemental composition (at %)			
CCTO	**Cu**	**Cd**	**Te**	**O**	**CCTO**	**Cu**	**Cd**	**Te**	**O**
0	-	47.2	51.8	-	**10**	14.6	34.6	45.4	3.6
2	3.2	45.7	51.0	-	**11**	16.6	33.8	46.8	1.9
3	4.0	44.8	51.1	-	**12**	17.7	33.1	44.5	3.5
5	6.1	41.0	48.6	4.1	**13**	23.9	28.3	41.6	5.2
6	7.5	41.1	48.0	1.6	**14**	19.8	30.3	44.0	5.2
7	9.1	38.8	46.1	5.7	**15**	20.6	30.4	44.1	3.7
8	10.0	37.7	45.8	6.3	**20**	26.0	25.8	38.4	9.2
9	12.4	35.1	47.2	4.5	**25**	31.2	21.8	34.5	11.9

As observed in the data, oxygen addition within the host matrix is detected after CCTO5 and remains below 6.3% for CCTO6-15 samples. It is assumed to be present in concentrations lower than the system´s detection limit. For CCTO20-25 it is presumed to be actively present in oxide compounds. The inverse behavior for Cu and Cd allows for the conclusion that Cu tends to substitute Cd in the CdTe matrix, with the possible formation of CuTe-like phases. This situation is favorable to the formation of Cu ohmic contacts on the CCTO thin films.

6.1.4. Structural characterization.

6.1.4.1. X-ray diffraction.

The X-ray diffractograms of Figure 6.5 were obtained through parallel beam configuration with a fixed incidence angle of 5.0 degrees. Power conditions were 30 kV and 20 mA of current impinging on a Cu target. Measurement parameters were steps of 0.02 degree with an acquisition time of 0.2 s.

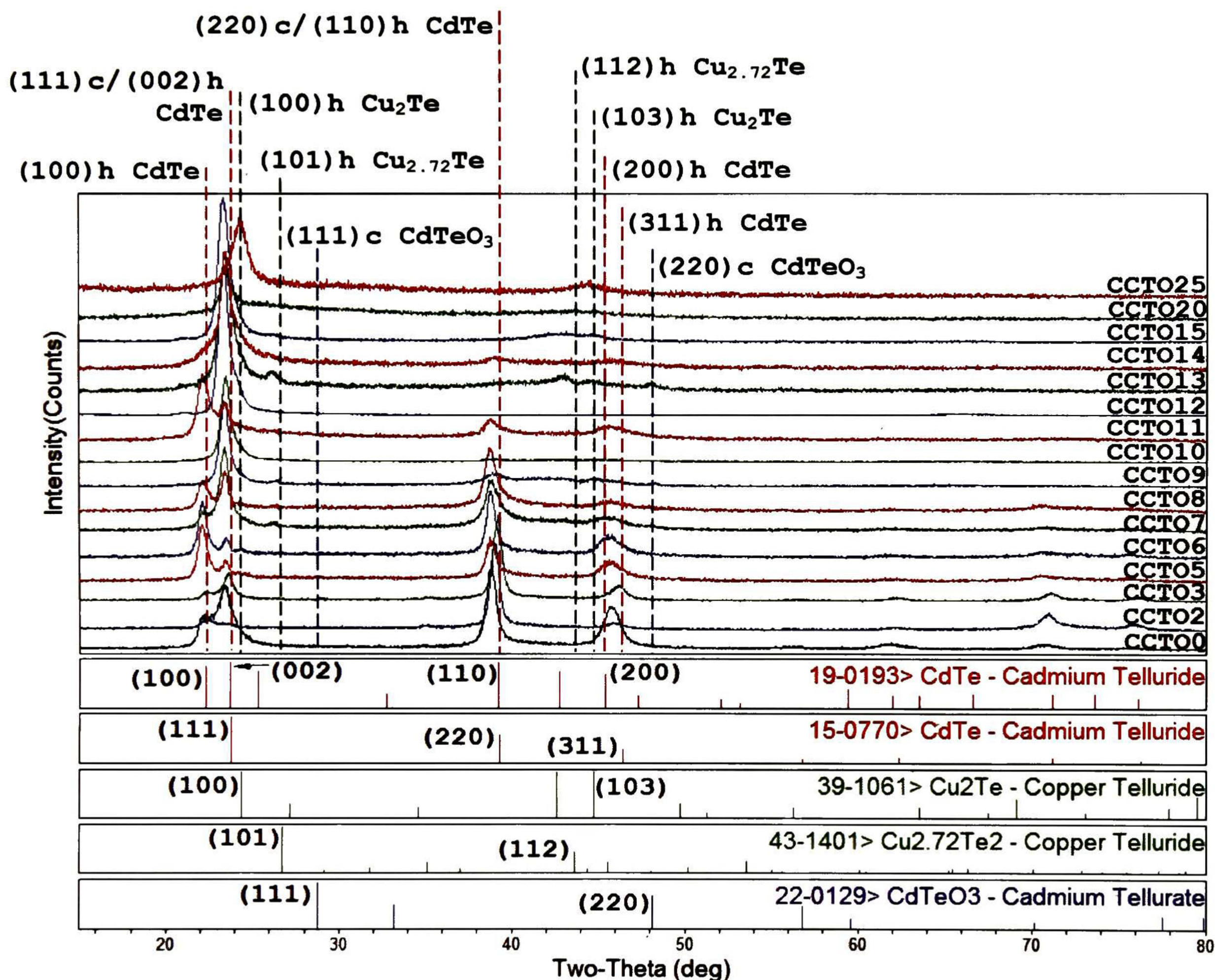

Figure 6.5. CCTO samples X-ray diffraction patterns.

All samples present polycrystalline arrangement with slight increment in their lattice parameters with respect to their corresponding reference PDFs. Since the films were grown on unintentionally heated substrates (Ts ~ 60 ˚C at the end of the deposition), it is reasonable to assume that the shift of

the peaks towards smaller angles is related to tensile stress in the films and/or to increased lattice parameters due to a high density of interstitial atoms. That is, the low thermal energy of the atoms arriving at the substrate does not suffice to achieve the minimum energy sites for the atoms.

Starting from the CCTO0 diffractogram, evident presence of both zinc-blende and wurtzite CdTe structures is observed. In addition overlaps of the PDFs reference diffraction lines at the most intense peaks for both phases are observed. CCTO2 does not show presence of a compound other than CdTe, but preferred orientations are encountered on the [110]h/[220]c (h for hexagonal and c for cubic) directions with a significant reduction of the (100)h, (002)h/(111)c peaks observed for CCTO0. This effect may be explained in terms of crystallites acquiring a stronger preferred orientation along the [110]h/[220]c directions upon Cu and O doping and/or to the allocation of atoms at sites on these planes within the cubic and hexagonal cells. This would increase the electronic charge density on these planes and therefore the intensity of these reflections. Figure 6.6 and Figure 6.7 show both CdTe wurtzite and zincblende structures fabricated with Vesta 3.2.1 [2]. The shown structures are an aid to illustrate some relevant planes obtained through the X-ray diffraction measurements.

CCTO3 shows a peak centered at the position $2\theta \approx 26.3°$ which is assumed to be the (101)h plane of the compound $Cu_{2.72}Te$, and also a wide band ($2\theta \approx 56.0°$) is observed, in agreement with the (202)h reflection of the Cu_2Te structure. CCTO5-6 reveal a peak centered at ~24.2° corresponding to the Cu_2Te (100)h plane. CCTO7 exposes two new clear features, located at ~43° and ~48°, corresponding to the (119)h $Cu_{2-x}Te$ plane and (220)c $CdTeO_3$ planes, respectively. CCTO8-20 show similar behavior, with increasing/decreasing intensities associated to the oxide compounds. CCTO12 shows the most intense peak measured for a CCTO sample performed in this work. It consists in the overlap of (002)h/(111)c peaks with a wide bread, comprising the reference lines of the found compounds in previous samples. CCTO25 shows an overall change of predominant phase, where the observed peaks correspond to (100) and (103) reflections of the Cu_2Te hexagonal structure.

The diffractograms of CCTO3-20 show not only a lattice distortion due to the random incorporation of Cu and O in the

CdTe lattice and to stress, but also short range tendencies of preferred orientations. The formation of Cu_xTe-like compounds with increasing CuO nominal concentrations and the formation of the Cu_2Te phase in CCTO25, imply Cu substitution for Cd atoms in the CdTe lattice. This is in agreement with EDS results, in which the Cu and Cd elemental compositions showed inverse behavior.

Theoretical calculations reported by C. Corwine, proved the existence of two low-energy unoccupied locations within the CdTe zincblende structure [3] that could be occupied by Cu and O atoms. These were located on the [111]c direction at $^1/_2$ and $^3/_2$ of the cube diagonal. These results show that the incorporation of Cu and O may lead to significant effects in the electronic charge density and electrical behavior of CdTe. When Cu is being interstitially introduced to the CdTe lattice, it locates near to Te ions at the center of the cubic structure and act as donors to the CdTe matrix. When Cd ions are substituted by Cu atoms, Cu ions act as acceptors in the CdTe sample.

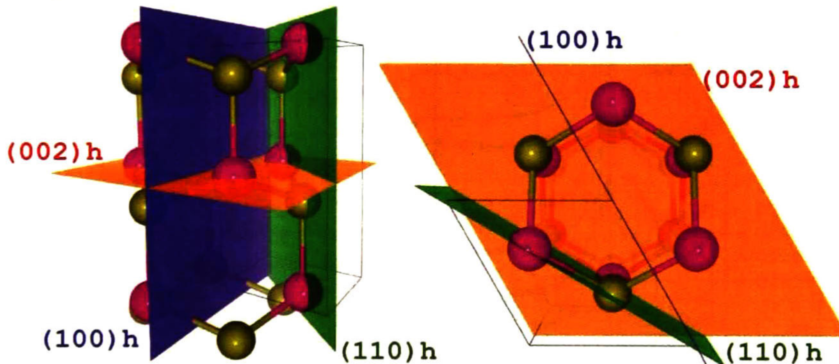

Figure 6.6. Some crystallographic planes in wurtzite structure.

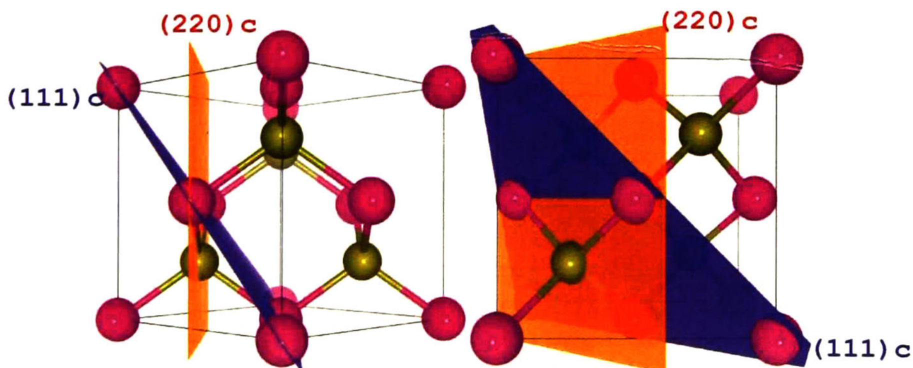

Figure 6.7. Some crystallographic planes in zincblende structure.

6.4.1.2. Raman scattering.

Raman scattering measurements shown in Figure 6.8 were obtained at RT with the He-Ne 632.8 nm laser line and using 1.34 mW.

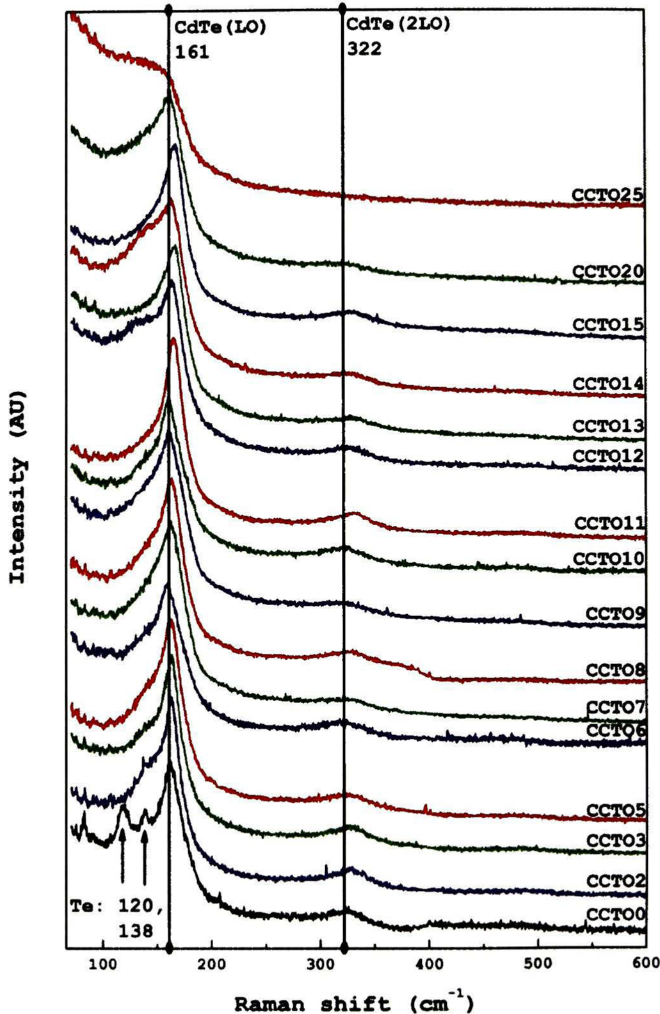

Figure 6.8. CCTO films Raman spectra.

Longitudinal-optical (LO) phonons (and their doublets 2LO) of CdTe are observed for CCTO0-20 samples, with slight displacements to lower photon energies. phonon modes of metallic Te at 120 and 138 cm^{-1} were found for CCTO0 (CdTe).

A wide band is observed for the CCTO25 at wavenumbers lower than 161 cm^{-1}, and the 2LO phonon is lost. These are due to the higher incorporation of Cu in the CdTe matrix, where Cu_2Te, $Cu_{2.72}Te$, $Cu_{2-x}Te$ and $CdTeO_3$ compounds are formed. Preliminary theoretical calculations for the lattice dynamics of Cu_2Te

reveal Raman shifts within the observed broad band (i.e. below 200 cm^{-1}) [4]. CCTO12 and CCTO14 also show bands within this range of wavenumbers. CCTO8 shows an evident band at the right of the 2LO phonon at 322 cm^{-1} that has not been identified yet. In Table 6.3 are listed the phonon modes with their respective Raman shifts in wavenumber units.

Table 6.2. CCTO samples Raman frequencies.

Mode	Raman shift (cm^{-1})
Cu_2Te	45-108, 201-218, 219-259
$CdTeO_3$	102, 137, 149
Te(A_1)	120
Te(E_{TO})	138
TeO_2	123, 155
CdTe(LO)	161
CdTe(2LO)	322

6.1.5. Optical characterization.

The measured reflectance spectra of 2 µm-thick CCTO samples are shown in Figure 6.9, where the substrate´s R characteristics are shown for comparison. A maximum value of ~35 % of reflection was measured for the CCTO15 sample. No T characteristics were detected for these samples during this characterization.

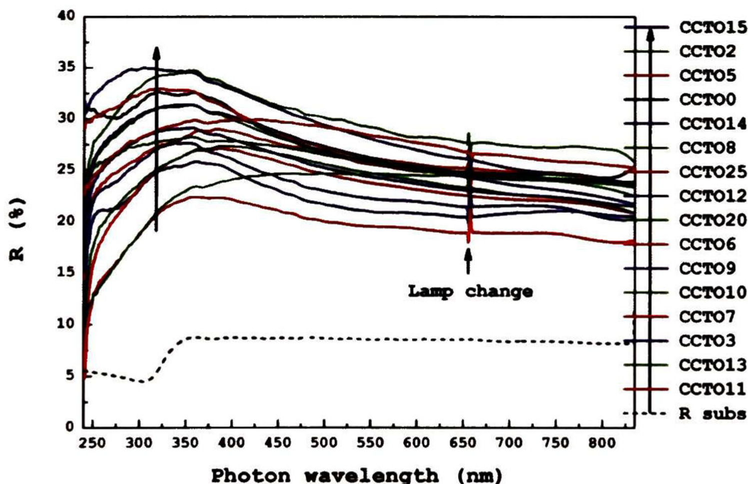

Figure 6.9. CCTO samples reflectance spectra.

A couple of features are observed in the measured R spectra of the CCTO0 sample centered on ~320 and ~360 nm. For clarity purposes Figure 6.10 shows the R dispersion with independent offsets in arbitrary units of intensity. The indicated

features are coincidental with the energies of the E_1 and $E_1+\Delta_1$ critical points of the electronic band structure of CdTe as shown in Figure 3.8 [5]. All cases reveal the E_1 and $E_1+\Delta_1$ critical points to a greater or lesser extent.

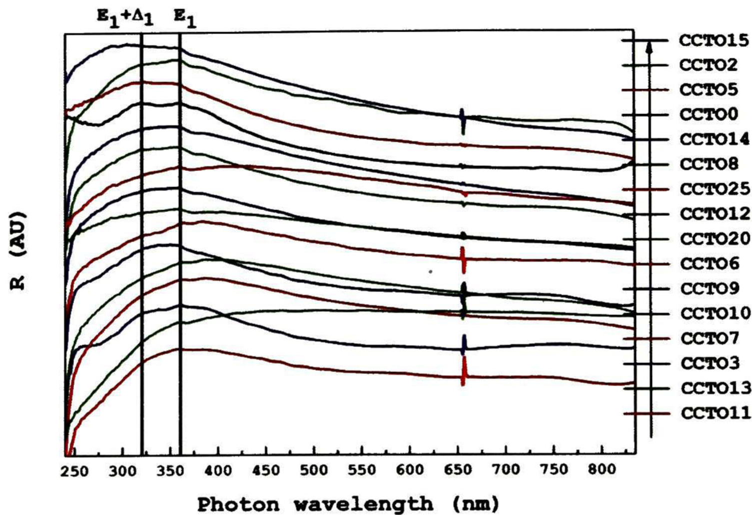

Figure 6.10. Cubic CdTe critical points in CCTO reflectance spectra.

In order to calculate band gap values, translucent CCTO thin films were fabricated with deposition times of 20 min with all the other described conditions held constant. Figure 6.11 shows the measured transmittance spectra for these films, where a maximum of ~50 % was recorded for the CCTO0 590 nm-thick sample.

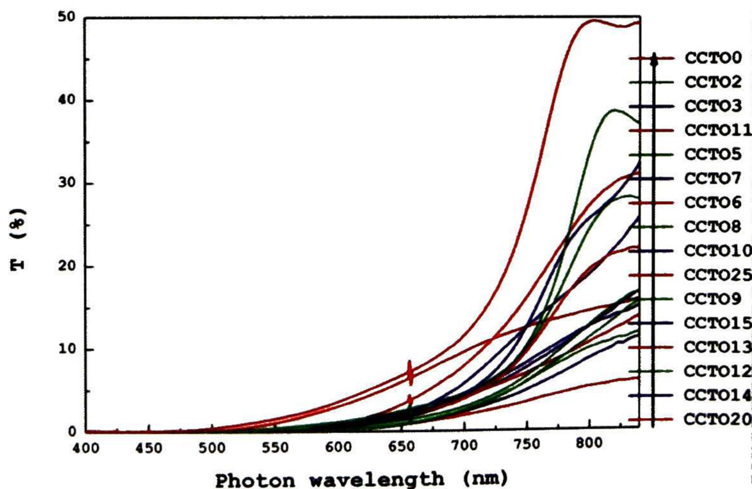

Figure 6.11. Translucent CCTO samples transmittance spectra.

Figure 6.12 illustrates the absorption edges for the films. According to the direct transitions between parabolic bands

model, linear fittings of the absorption edges and extrapolations to the photon energy axis were performed to estimate the band gap values of the CCTO thin films.

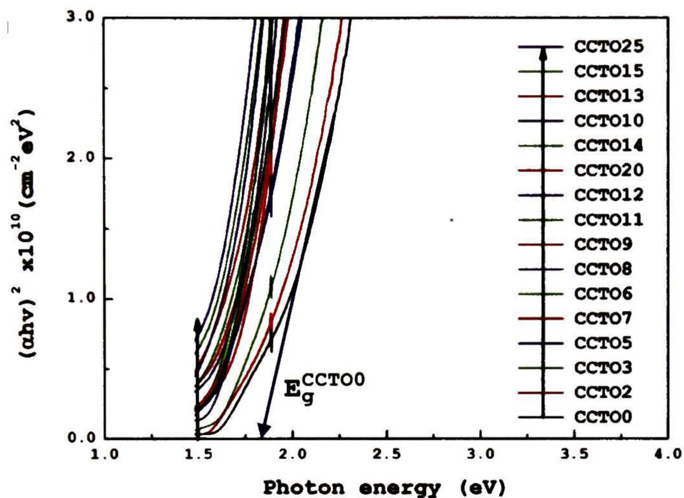

Figure 6.12. CCTO samples fundamental edges of absorption.

Table 6.3. CCTO films band gap values.

CCTO	E_g (eV)		CCTO	E_g (eV)
0	1.76		10	1.48
2	1.74		11	1.57
3	1.60		12	1.55
5	1.53		13	1.46
6	1.56		14	1.51
7	1.60		15	1.45
8	1.55		20	1.50
9	1.55		25	1.45

Table 6.3 lists the band gap values. An evident shift of energy of ~0.2 eV is observed in the band gap for the CCTO0 sample (pure CdTe), whose accepted single cubic crystal value is 1.5 eV and for the hexagonal structure has been calculated as 1.78 eV [6]. The experimental value for the CdTe film (1.76 eV) may be due to a combination of factors, such as the presence of the hexagonal phase and to electronic confinement caused by the small grain sizes obtained during the films growth at RT. According to the deconvolution applied to the diffractogram of sample CCTO0 (pure CdTe), crystallites with sizes of ~50 and ~110 Å were estimated for the cubic and hexagonal phase of CdTe, respectively. It can also be observed a general tendency of E_g to decrease upon the CuO nominal concentration in the target was higher. This behavior was associated to the influence of the formed $Cu_{2-x}Te$-like

compounds which has been shown to have a transmission window between 400 and 1000 nm, depending on the copper telluride polytype.

A second transmittance measurement was performed in the range of 190 - 3300 nm with the Cary 5000 equipment. Figure 6.13 shows the measured T spectra of the translucent CCTO samples. Absorption of light in the near-infrared region (1000 - 25000 nm) is observed with a general trend of reduction from CCTO0 to CCTO25. This effect is consistent with absorption by surface plasmons at the boundaries between the metallic aggregates and the semiconducting CdTe matrix. Figure 6.14 shows the CCTO fundamental edges of absorption, where a linear fit for the CdTe band gap calculation is observed.

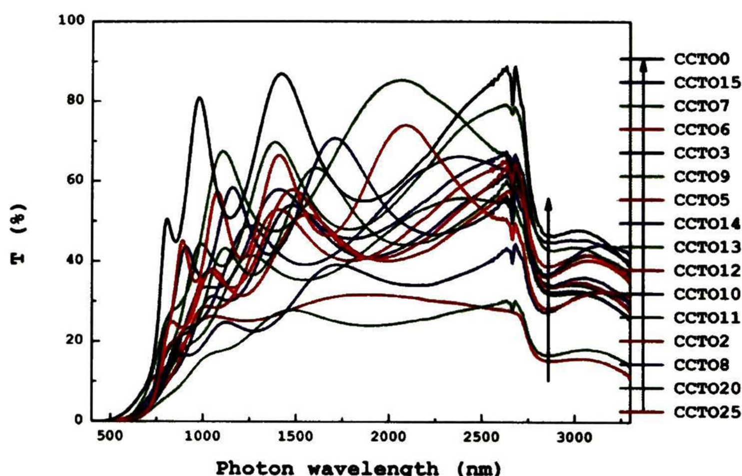

Figure 6.13. CCTO samples UV-VIS-NIR transmittance spectra.

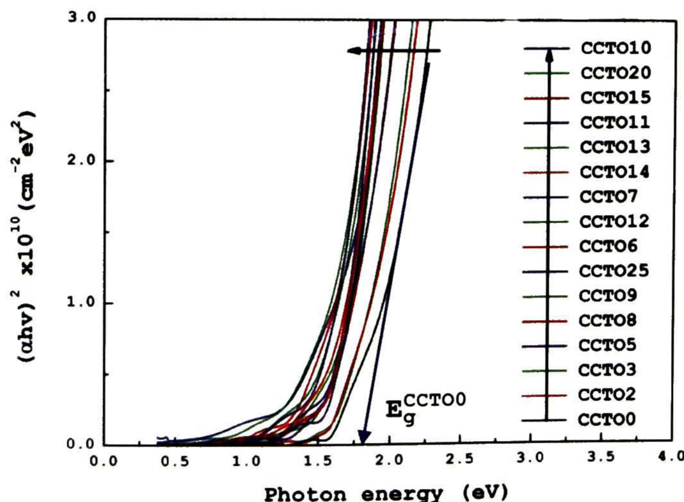

Figure 6.14. CCTO samples edges of absorption.

The estimated gap values are listed in Table 6.4. These values are in agreement with the previous calculations, following the general tendency of reduction upon the CuO nominal concentration in the target.

Table 6.4. CCTO films band gap values.

CCTO	E_g (eV)		CCTO	E_g (eV)
0	1.78		**10**	1.55
2	1.69		**11**	1.58
3	1.73		**12**	1.61
5	1.61		**13**	1.53
6	1.57		**14**	1.56
7	1.60		**15**	1.57
8	1.59		**20**	1.54
9	1.59		**25**	1.60

6.1.6. Electrical characterization.

6.1.6.1. Hot-point probe.

Measured surface potential differences as a function of time are shown in Figure 6.15. Negative steps reveal *p*-type behavior for the CCTO10-25 samples. Positive steps for CCTO0-9 indicate unintentional *n*-doping by the corresponding CuO nominal concentrations, with concluding exclusion from solar cells.

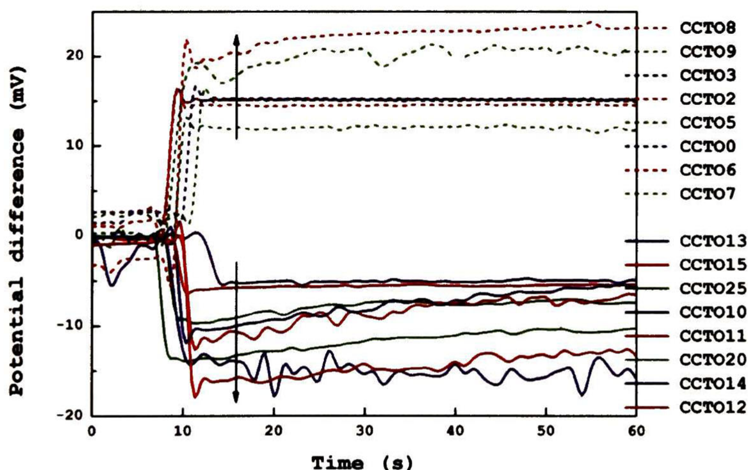

Figure 6.15. CCTO films hot-point probe measured voltages.

The CCTO10-25 samples possess significant influence of CuTe-like compounds (*p*-type semiconductors), which explains the predominant population of holes as the majority charge carriers detected through this characterization.

It is worth mentioning that the latter results are in disagreement with previous reports about the type of majority charge carriers of samples CCTO0-9. Hall effect measurements with adequate ohmic contacts consists in a method to clarify this opposite behavior observed through the hot-point probe system, which may encounter difficulties upon the resistivity values of the CCTO0-9 values.

6.1.6.2. Work function.

Measured electron work functions by KPFM are listed in Table 6.5, and a lay out of their behavior is shown in Figure 6.16.

Table 6.5. CCTO work functions.

CCTO	Φ (eV)
10	4.73
11	4.99
12	5.17
13	5.78
14	6.18
15	6.38
20	5.24
25	4.95

A tendency to increase from CCTO10-15 is observed. These results establish a new CCTO surface property modified as a function of the CuO nominal concentrations.

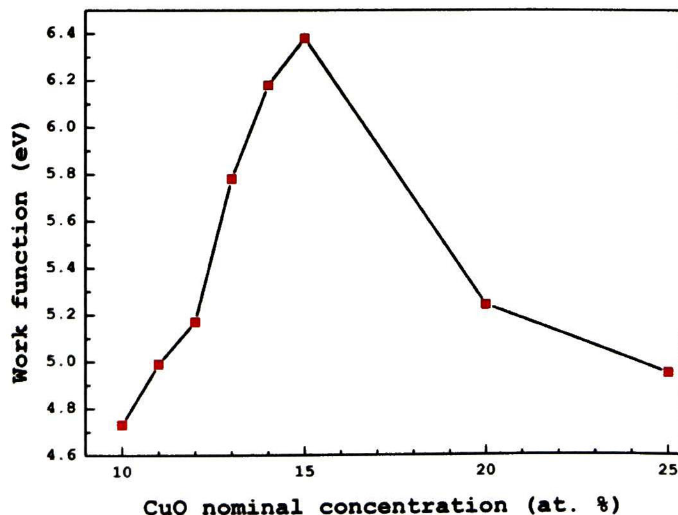

Figure 6.16. CCTO films work functions.

6.2. Cu front contact.

6.2.1. Cu/*p*-CCTO junction

Flat band schemes of Figure 6.17 illustrate the band alignment for the Cu/*p*-CCTO junction where Φ_{Cu}=4.65 [7]. Potential barriers will arise within the *p*-type CCTO once the junction with Cu is carried out, with the intention to avoid hole diffusion into the metallic contact.

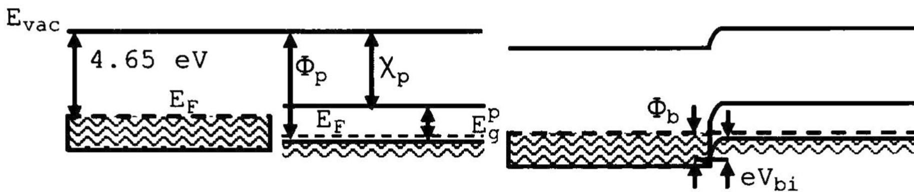

Figure 6.17. Cu/*p*-CCTO junction. (a) Before and (b) after contact.

For the CCTO measured electron work functions and band gaps, the crystal electron affinity value must be known, in order to calculate Schottky and built-in potentials for the Cu/*p*-CCTO junctions. Nevertheless, Cu has been extensively reported as an ohmic contact to CdTe, due to its diffusion and formation of CuTe-like compounds that enhance this junction.

6.2.2. Thickness.

Measured thickness values of 70 nm and geometries for the 10 Hall effect samples fabricated through shadow masks are depicted in Figure 6.18.

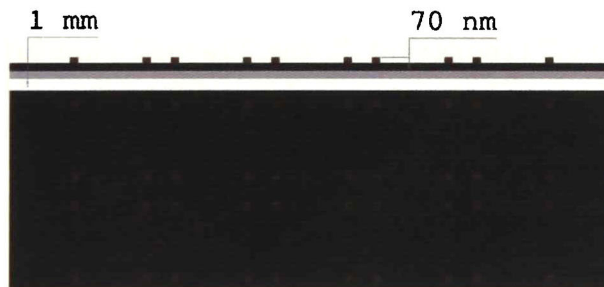

Figure 6.18. CCTO Hall effect samples 3-D design. (a) Lateral and (b) planar views

6.2.3. Electrical characterization.

I-V and Hall effect measurements were carried out, with different current values within the range of 1 nA to 21 µA. Averaged values for the measured concentration of majority charge carriers, resistivity, conductivity and mobility of the CCTO samples are listed in Table 6.6.

Table 6.6. CCTO samples electrical parameters.

CCTO	ρ (Ω·cm)	n, p (cm^{-3})	σ $(Ω·cm)^{-1}$	µ ($cm^2(Vs)^{-1}$)
0	-	-	-	-
2	-	-	-	-
3	7.12E1	2.28E18	1.40E-2	5.10E-2
5	8.08E2	8.69E15	2.91E-3	2.36E1
6	1.23E3	5.18E15	1.61E-3	5.91
7	1.58E2	2.99E17	6.33E-3	2.72E-1
8	5.55E2	3.76E16	2.40E-3	5.29
9	8.31E1	2.17E18	1.2E-2	6.63E-2
10	1.05	2.44E19	9.51E-1	4.98E-1
11	1.2E1	2.5719	7.85E-2	4.49E-2
12	2.26E-1	4.74E19	4.41	1.43
13	7.95E-2	4.55E19	1.25E1	4.92
14	6.67E-1	1.35E20	1.49	3.75E-1
15	6.60E-2	2.40E20	1.51E1	2.15
20	5.19E-2	7.09E19	1.92E1	6.19
25	2.44E-2	6.63E19	4.08E1	11.6

CCTO0-2 samples were found to have resistivity values over the limit embedded by the characterization system. Behaviors for the electrical parameters are shown in Figure 6.19 and Figure 6.20, where blue and red squares represent the *n*-CCTO and *p*-CCTO samples, respectively. General trends are observed particularly in resistivity (decrease) and majority charge carrier density (increase). The large carrier density for CCTO15-25 shows the large influence on the electronic properties of these films due to the increasingly larger Cu and O concentrations.

The type of majority charge carriers for the different nominal concentrations of CuO in the target could not be clarified through Hall effect measurements with Cu contacts. The measured sign for the type of free charge carriers of the samples did not held constant over a wide range of current values. This is associated with non-ideal ohmic behavior for the Cu/CCTO junction, so an optimum ohmic contact on the

CCTO0-25 samples must be met in order to clarify the observed discrepancy of the majority charge carrier type for CCTO0-9.

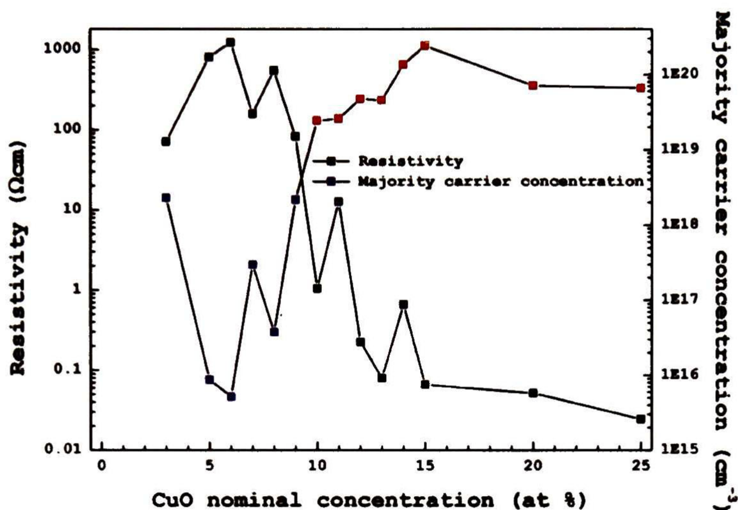

Figure 6.19. CCTO films resistivity and majority charge carrier concentration.

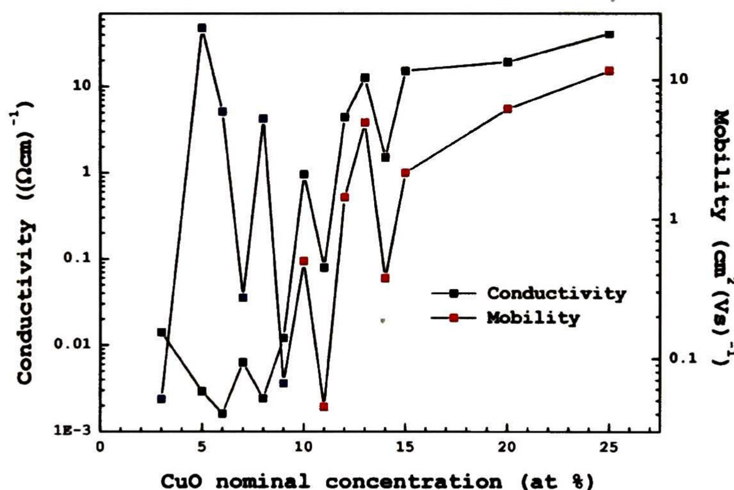

Figure 6.20. CCTO films conductivity and mobility.

6.3. ZnO thin films.

6.3.1. Topography.

The conditions exposed in section 4.3, result in thickness values for the ZnO thin films of 500 nm at the substrate´s center and 400 nm at opposite ends of the substrate. Figure 6.21 depicts both cross-sectional and planar views of the samples.

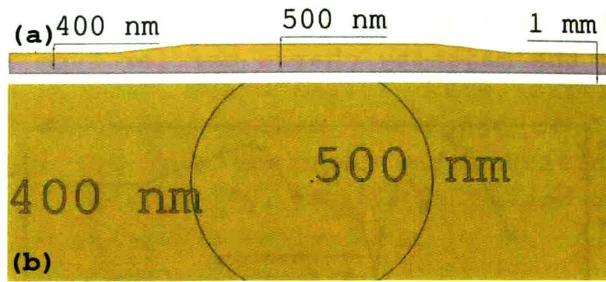

Figure 6.21. Window layer 3-D design. (a) Thickness and (b) approximated planar distribution.

Topographical images of a ZnO sample are shown in Figure 6.22. Sphere-like particles with sizes between 100 and 200 nm are observed with average RMS surface roughness lesser than 2.37 nm.

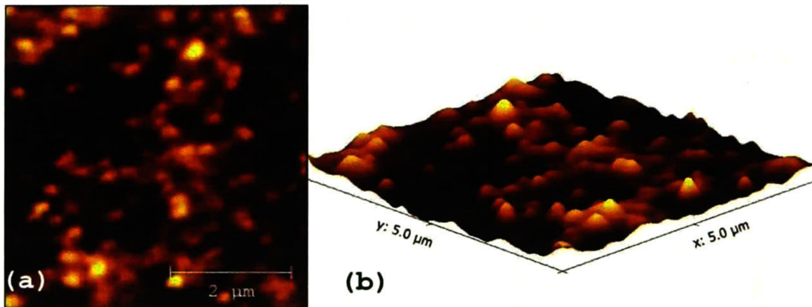

Figure 6.22. ZnO film topographical map. (a) 2-D and (b) 3-D view.

6.3.2. Morphology.

Figure 6.23 shows a ZnO film surface micrograph obtained, where a smooth surface can be observed.

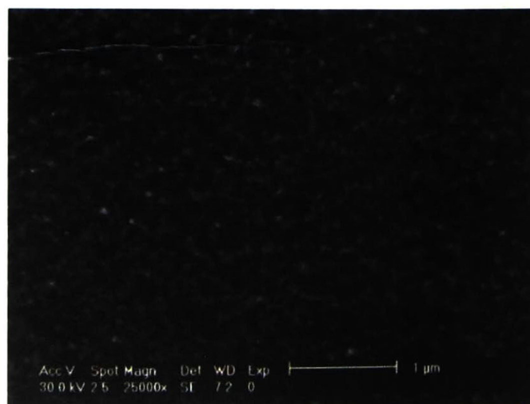

Figure 6.23. ZnO film ESEM morphology.

6.3.3. Structural characterization.

6.3.3.1. X-ray diffraction.

The diffraction patterns shown in Figure 6.24 correspond to structure (zincite) with cell parameters a = b = 3.26 Å and c = 5.26 Å, and reveals a [002] preferred orientation with a FWHM of 0.8464.

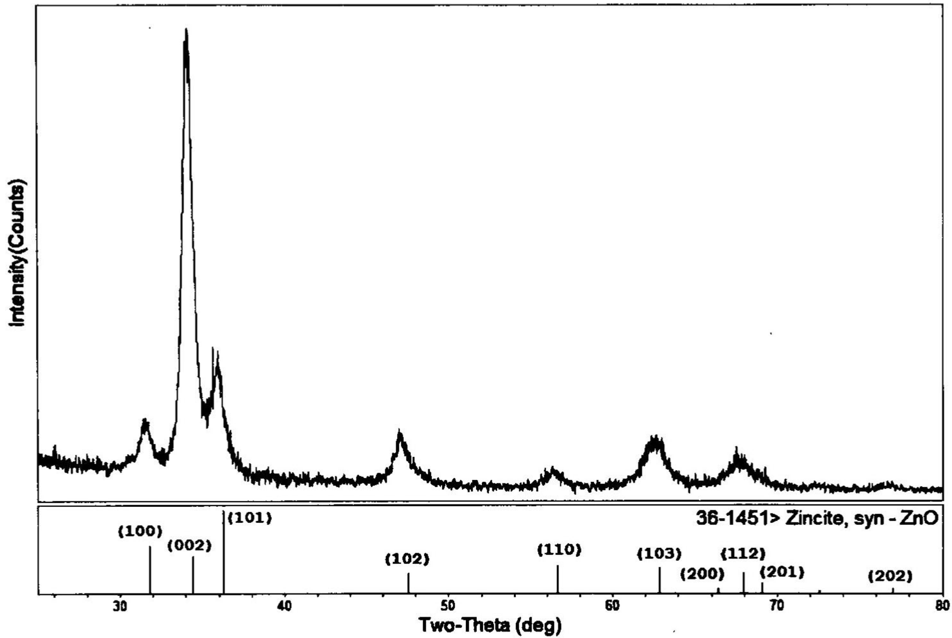

Figure 6.24. ZnO film X-ray diffraction pattern.

The (002)h planes with interplanar distances of 2.62 **Å** are shown in Figure 6.25, where the hexagonal structures are constructed, parallel to the substrates surface. Crystallite size were calculated to be ~104 ± 1 Å.

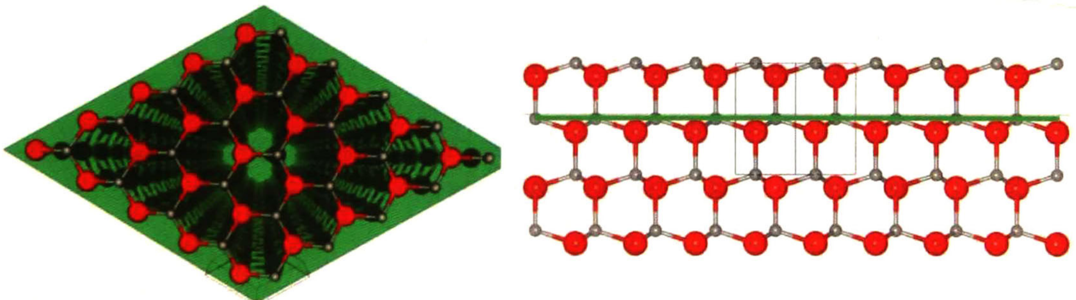

Figure 6.25. Zincite [002]h preferential orientation.
(a) planar and (b) lateral views.

6.3.3.2. Raman scattering.

Measured Raman spectrum acquired with 514.5 nm laser line is shown in Figure 6.26. In Table 6.7 are listed the observed Raman frequencies in cm^{-1} units of the ZnO thin film and their corresponding vibrational modes. The peak observed at 339 cm^{-1} has been identified as the second-order difference process $E_2^{high} - E_2^{low}$ [8].

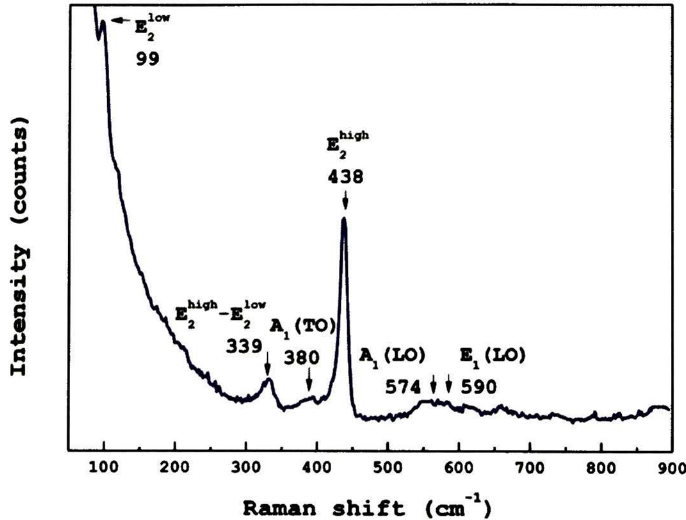

Figure 6.26. ZnO sample Raman spectrum.

Table 6.7. ZnO Raman frequencies.

Mode	Raman shift (cm^{-1})
E_2^{low}	99
$E_2^{high} - E_2^{low}$	339
A_1(TO)	380
E_1(TO)	410
E_2^{high}	438
$2B_1^{low}$	536
A_1(LO)	578
E_1(LO)	584

6.3.4. Optical characterization.

The reflectance and transmittance spectra of the window layer are shown in Figure 6.27. The observed oscillations are result of constructive and destructive interference between light beams from the film/air and film/substrate interfaces.

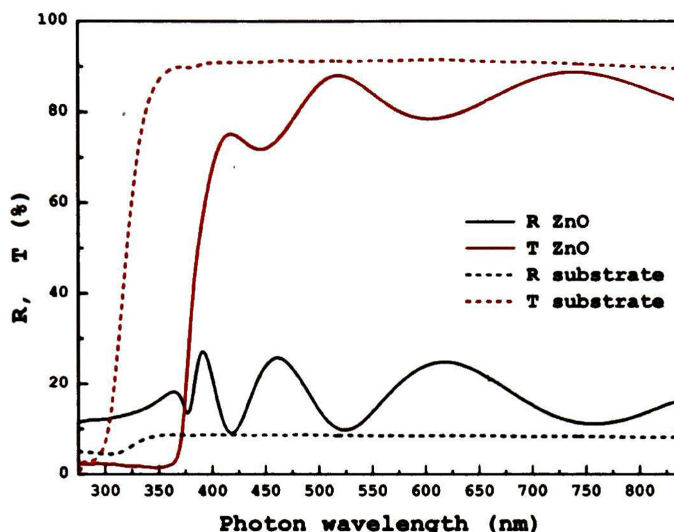

Figure 6.27. ZnO film reflectance and transmittance spectra.

Figure 6.28 depicts the fundamental absorption edge for the ZnO direct gap semiconducting samples. A judicious linear fit of the absorption edge provides a band gap value of 3.27 eV, in good agreement with the reported value of 3.37 eV [9]. This implies transparency in the visible region.

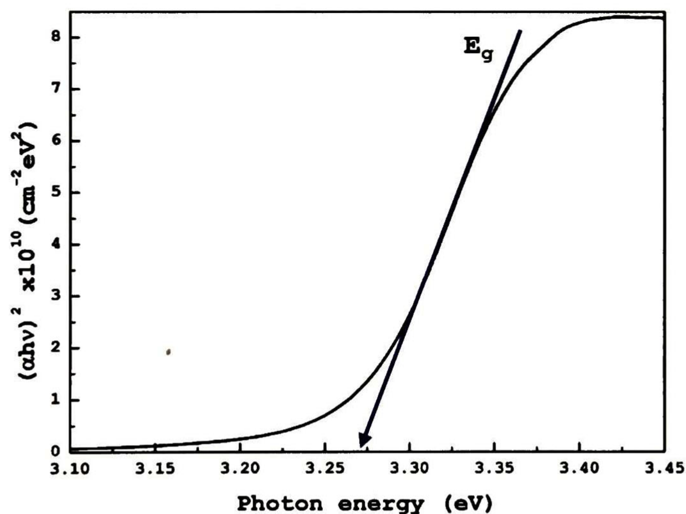

Figure 6.28. ZnO sample fundamental absorption edge and linear fit to determine E_g.

6.3.5. Electrical characterization.

Figure 6.29 shows a positive potential in the hot-point probe measurement. This is the *n*-type typical behavior for Zno thin films grown by RF sputtering. Several research groups have

reported *p*-type ZnO thin films, with issues on reproducibility.

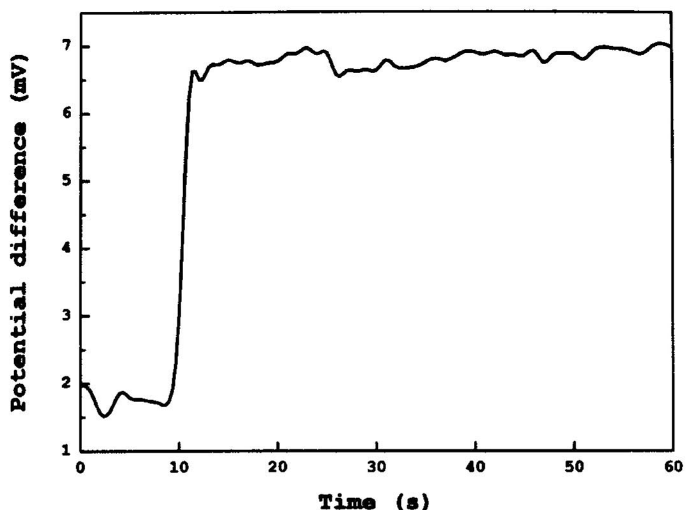

Figure 6.29. ZnO film hot-point probe voltage as a function of time.

6.3.5.1. Work function.

The measured contact potential differences maps are shown in Figure 6.30 for gold (a) and ZnO (b).

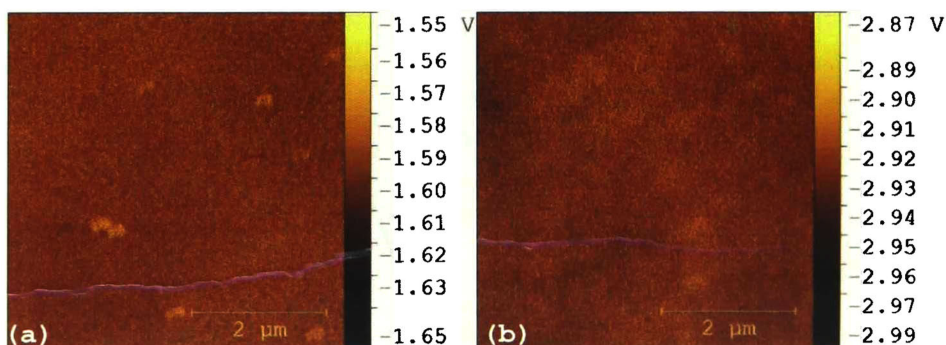

Figure 6.30. Contact potential difference images. (a) Gold and (b) ZnO thin film.

The average value for the electron work function of the ZnO film was determined to be 4.0 eV. This is lower than the reported value of 4.45 eV.

6.4. Ti/Al contact.

6.4.1. *n*-ZnO/Ti/Al junction.

Flat band schemes for the corresponding junction are shown in Figure 6.31, for ZnO, Ti and Al before and after contact is performed where $\Phi_{Ti} = 4.33$ eV and $\Phi_{ZnO} = 4.0$ eV. The configuration Ti/Al is reported as ohmic contact to ZnO [10].

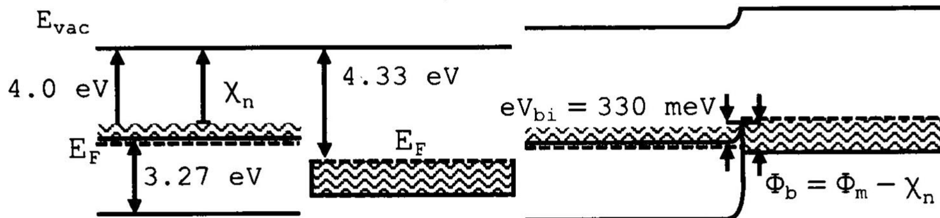

Figure 6.31. *n*-ZnO/Ti junction. (a) Before and (b) after contact.

A built-in potential of 0.33 eV arises within the window layer to prevent electron diffusion into the metal. Value for the ZnO electron affinity must be known in order to calculate the Schottky barrier, where the reported χ_{ZnO} values are greater than the measured work function.

6.4.2. Thickness.

The conditions exposed in section 4.4, resulted in thickness values for the Ti thin films of around 500 nm. Values of 1.5 µm at the substrate center and 1 µm at the substrate ends were found for the Al thin films. Figure 6.30 depicts both a cross-sectional and planar views, for the Ti/Al thin films depositions.

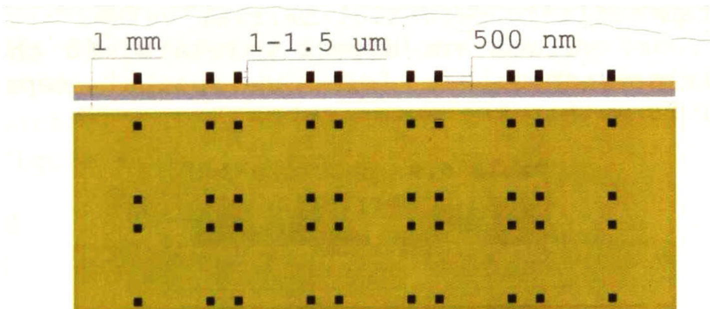

Figure 6.32. ZnO Hall effect samples 3-D design. (a) Lateral and (b) planar views.

6.4.3. Electrical characterization.

The electrical properties of the n-ZnO thin films with Ti/Al are resumed in Table 6.8, for several thermal treatments. Accurate and constant values for the majority carriers' concentration, resistivity and mobility are indicators of ohmic metallic contacts.

Table 6.8. Electrical parameters of ZnO thin films.

T.T. in air	n (cm^{-3})	ρ (Ωcm)	μ ($cm^2V^{-1}s^{-1}$)
-	1.71×10^{19}	1.09×10^{-1}	4.15
100 °C x 30 min	5.82×10^{19}	2.09×10^{-2}	10.60
150 °C x 10 min	1.94×10^{19}	1.55×10^{-1}	3.10
200 °C x 30 min	3.83×10^{18}	2.31	5.66

6.5. Heterojunction.

6.5.1. *p*-CCTO/*n*-ZnO.

The band alignement prediction at the depletion region of the *p*-CCTO/*n*-ZnO junction is schematized in Figure 6.33.

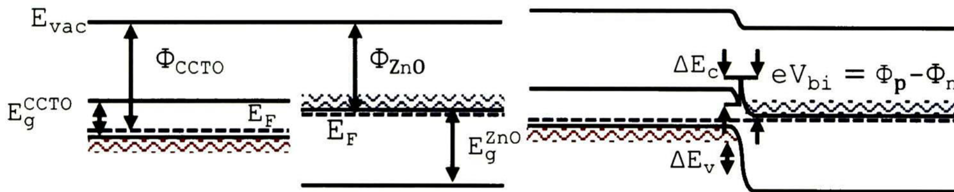

Figure 6.33. *p*-CCTO/*n*-ZnO heterojunction. (a) Before and (b) after contact.

The calculated built-in potential barrier values are listed in Table 6.9. These values are directly related to the built-in electric field responsible for the spatial separation of charge carriers within the solar cell.

Table 6.9. *p*-CCTO/*n*-ZnO junction barrier height.

CCTO	eV_{bi} (eV)
10	0.73
11	0.99
12	1.17
13	1.78
14	2.18
15	2.38
20	1.24
25	0.95

6.6. Heterojunction solar cell.

6.6.1 Efficiency.

The configuration #1 of the fabricated superstrate-type solar cell is illustrated in Figure 6.34. There one may observe 48 0.2 square mm solar cell structures. Figure 6.35 shows the measured dimensions for the #1 through a cross-sectional view, where the values at right are for the thicker regions (center) and the values at left correspond to the thinner regions (edges).

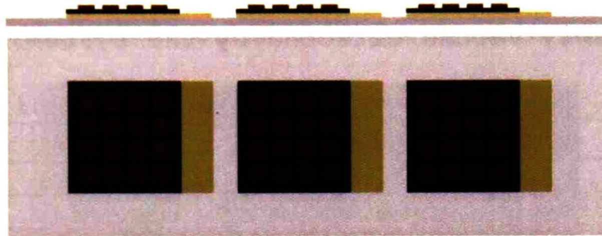

Figure 6.34. Configuration #1 solar cells 3-D design. (a) Lateral and (b) planar views.

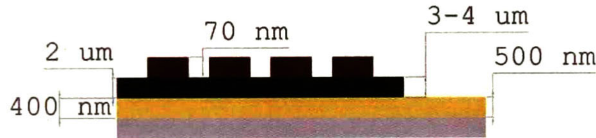

Figure 6.35. Configuration #1 solar cell thickness values.

In order to avoid damage to the solar cells by short-circuiting the device due to the positive contact placement, configuration #2 (first proposed by G. Wary et al. [11]) was fabricated. Eight research-size solar cells are depicted in Figure 6.36. The measured dimensions for the CCTO, ZnO and Cu depositions are equivalent with the ones previously reported. The back contact to ZnO consists of a 60 nm-thick Al layer, as shown in Figure 6.37.

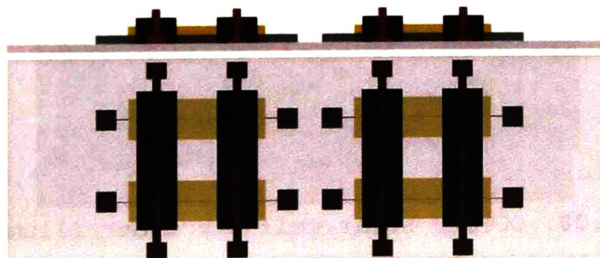

Figure 6.36. Configuration #2 solar cells 3-D design. (a) Lateral and (b) planar views.

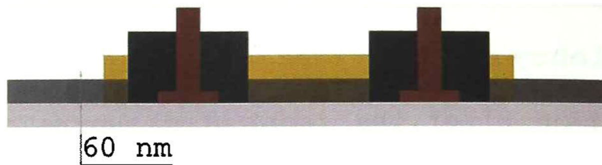

Figure 6.37. Configuration #2 solar cell lateral view scheme.

The measured values for open-circuit voltage, short-circuit resistance and shunt resistances are listed in Table 6.10. Conversion efficiency values were obtained of the order of 10^{-4}, 10^{-5} and 10^{-6} % for CCTO10, CCTO13-14 and CCTO15 solar cells, respectively. It is assumed that these represent the higher efficiency values detected by the system.

Table 6.10. Heterojunction CCTO-based solar cell parameters.

CCTO	V_{oc} (mV)	I_{sc} (mA/cm^2)	R_s (Ω·cm^2)	R_{sh} (Ω·cm^2)
10	2.44	63.0E-3	-	14.58E3
11	139.7	-	-	9.07E3
12	45.38	-	-	297.3E3
13	4.58	2.01E-6	-	4.76E4
14	3.0	7.55E-6	-	1.0E3
15	3.6	7.56E-3	-	4.24E3
20	22.0	-	-	4.03E4
25	-	-	-	3.45E2

Figures 6.38-45 illustrates the measured J-V relations under illumination for CCTO10-25 solar cells following configuration #2. It is worth mentioning that dark J-V plots were similar to the plots acquired under illumination.

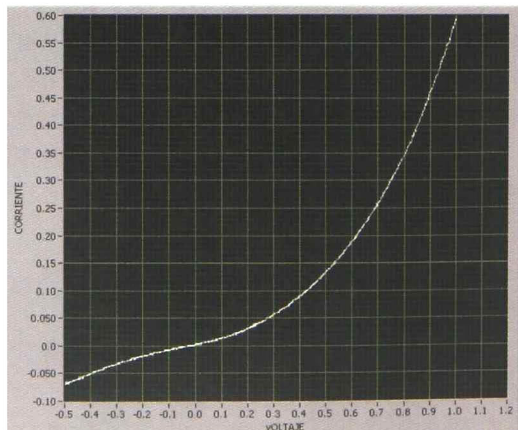

Figure 6.38. CCTO10 solar cell J-V under illumination.

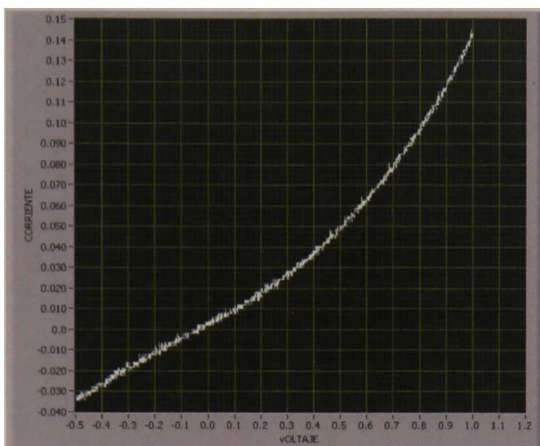

Figure 6.39. CCTO11 solar cell J-V under illumination.

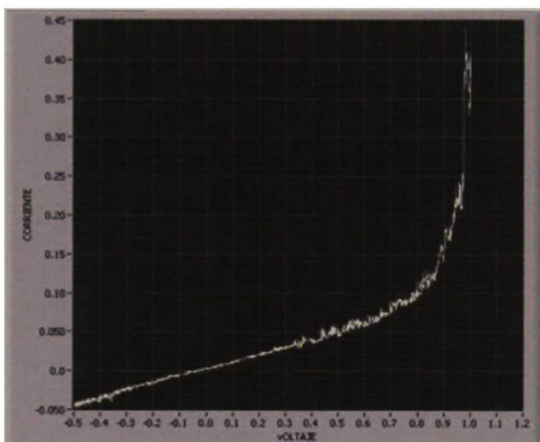

Figure 6.40. CCTO12 solar cell J-V under illumination.

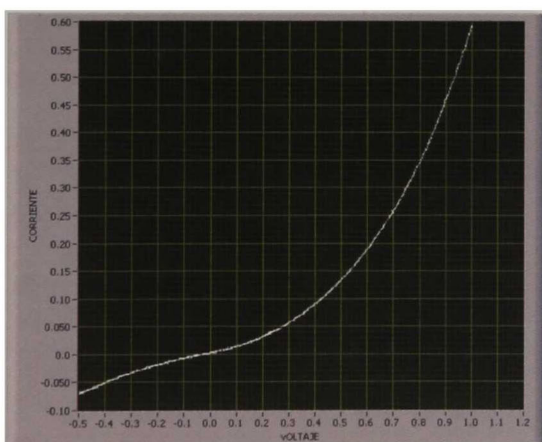

Figure 6.41. CCTO13 solar cell J-V under illumination.

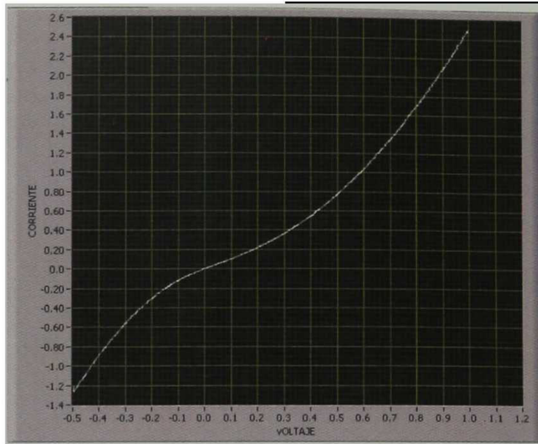

Figure 6.42. CCTO14 solar cell J-V under illumination.

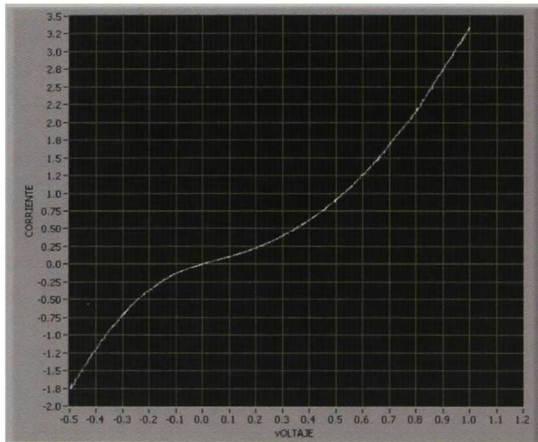

Figure 6.43. CCTO15 solar cell J-V under illumination.

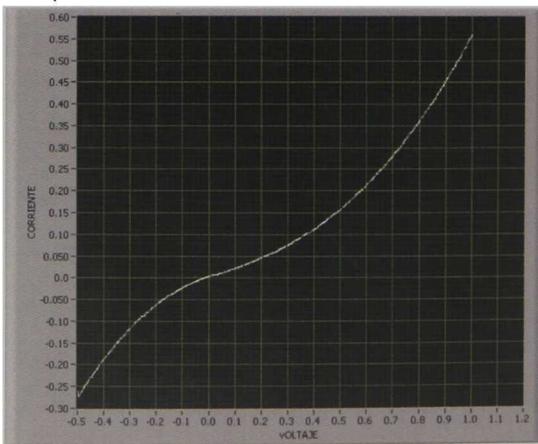

Figure 6.44. CCTO20 solar cell J-V under illumination.

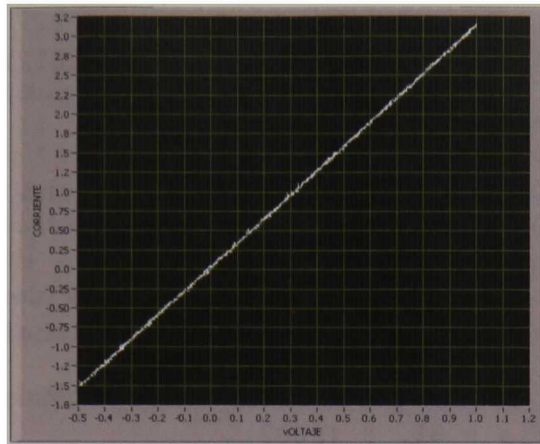

Figure 6.45. CCTO25 solar cell J-V under illumination.

The observed J-V behavior for all the heterojunction solar cells (configuration #2) was basically the same under dark conditions.

As listed in Table 6.10, it is clear that negligible currents were measured under illumination. In other words, photo-generated electrons could not flow out of the solar cell structure. This may be due to poor (Cu and Al) contacts diffusion into the CCTO and ZnO layers. Because of the RT conditions of the substrate during the fabrication process, Cu and Al atoms do not present high thermal energy to generate diffusion currents into the layers. Also, disorder and defects such as large grain boundary densities (small grain sizes) present are detrimental for electron transport through both *p-n* heterojunction and metal/semiconductor junctions.

References.

[1] David Nečas, Petr Klapetek, Cent. Eur. J. Phys. **10,** 1 (2012).

[2] K. Momma and F. Izumi, J. Appl. Crystallogr. **44** (2011).

[3] C. Corwine, PhD thesis (2006).

[4] Y. Zhao, X. Jind and W. Su, J. Mol. Struct. **87,** 43, (2002).

[5] A. Mendoza-Galván, S. Jiménez-Sandoval, J. Carmona-Rodríguez, Thin Solid Films **519,** 9 (2011).

[6] M. Ribeiro, Jr., L. R. C. Fonseca, T. Sadowski and R. Ramprasad. J. of Appl. Phys. **111**, 073708 (2012).

[7] H. B. Michaelson, J. of Appl. Phys. **48**, 11 (1997).

[8] R. Cuscó, E. Alarcón-Lladó, J.Ibáñez and L. Artús. Phys. Rev. B **75**, 165202 (2007).

[9] H. Morkoc and Ü. Özgur. Zinc Oxide: Fundamentals, Materials and Device Technology. Wiley, Weinheim. (2009)

[10] S. Y. Kim, H. W. Jand, J. K. Kim, C. M. Jeon, Journal of Electronic Materials **31**, 8 (2002).

[11] G. Wary, T. Kachary and A. Rahman. Intl. J. of Thermophysics **27**, 1 (2006).

7. Closure.

7.1. Conclusions.

Solar cell structures were prepared entirely by rf sputtering without intentionally heating the substrate. The absorbing layer was deposited using composite targets made of powder mixtures of CdTe and CuO with different concentration ratios. The window layer was a ZnO film for all cases. The tested cells were prepared in superstrate configuration.

7.1.1. CCTO thin films: absorbing layer.

The growth conditions, basically no intentionally heated substrate, produced low-surface-roughness. The maximum RMS value was 4.13 nm for sample CCTO6, while the minimum, of film CCTO25, was smaller than 1 nm.

The difference in thickness between the central region of the glass substrate (2.5 x 7.5 cm^2) and its extremes fluctuated between 1-2 microns.

The surface morphology (particle geometry and size) was found to depend strongly upon the CuO concentration in the target.

The observed inverse behavior of the Cu and Cd elemental concentrations in the films led to the interpretation that Cu atoms tend to substitute for Cd in the CdTe lattice.

The X-ray diffraction results showed that the growth of the films occurred preferentially along certain crystallographic directions. Specifically, along the [110]h, [002]h/[111]c, and [110]h/[220]c directions of the cubic and hexagonal phases of CdTe.

Formation of hexagonal Cu_2Te and $Cu_{2.72}Te$ and cubic $CdTeO_3$ was observed from the lowest CuO nominal concentration (2 at.%). Strong influence of Cu_2Te in the sample with 25 at.% of CuO nominal concentration led to the absence of other compounds in the measured diffractogram of the corresponding thin film.

The LO and 2LO vibrational modes of CdTe were observed for CCTO0-20 samples. Vibrational modes of metallic Te were found in the Raman spectrum of the undoped CdTe film. The sample with [CuO]=25 at.% showed a broad shoulder around 161 cm^{-1},

with no evidence of the LO and 2LO modes of CdTe. This feature was associated to $Cu_{2-x}Te$ compounds based on preliminary theoretical calculations of the Raman modes for Cu_2Te which showed that all the normal modes have frequencies below 200 cm^{-1}.

Optical spectroscopy revealed no transmittance signal for the thicker regions (3-4 μm) of the CCTO samples. The reflectance spectra showed a feature corresponding to the E_1 critical point of the electronic band structure of cubic CdTe.

It was found that CuO nominal concentrations above 10 at.% enhanced the *p*-type conductivity of the films.

The electron work functions of the CCTO samples were between 4.73 and 6.38 eV. The maximum value corresponded to [CuO]=15 at.%.

Linear I-V relations in the 4-point probe method revealed ohmic behavior for the Cu metallic contacts on the CCTO films.

Measured values of majority charge carrier concentration (10^{15}-10^{20} cm^{-3}), conductivity (10^{-3}-10^{1} $\Omega^{-1}\cdot cm^{-1}$) and mobility (10^{-2}-10^{1} $cm^2V^{-1}s^{-1}$ for *n*-type and *p*-type) showed a general tendency to increase with the CuO nominal concentration in the target.

7.1.2. ZnO thin films: window layer.

The rms surface roughness for a typical ZnO film was 2.37 nm.

The films grew preferentially oriented parallel to the [002]h direction of the zincite structure of ZnO, with crystallite sizes of ~71 Å.

Typical values for reflectance and transmittance were ~10% and ~80%, respectively, in the visible. From the fundamental absorption edge the band gap of the ZnO films was determined to be 3.27 eV.

The ZnO *n*-type conductivity was demonstrated through hot-point probe tests.

The electron work function value of a representative ZnO sample was measured as 4.0 eV, lower than the typical reports for ZnO thin films (4.45 eV).

Majority charge carrier concentrations and resistivity values for the as-deposited ZnO samples were of the order of 10^{19} cm^{-3} and 10^{-1} $\Omega\cdot cm$, respectively. The resistivity decreased to 10^{-2} $\Omega\cdot cm$ after a thermal treatment of 100 °C for 30 min.

7.1.3. Heterojunction solar cells.

Conversion efficiencies for the fabricated solar cells following configuration #2 were obtained within the range of 10^{-4}-10^{-6} % with no evident change after thermal treatments in air for 10 minutes and temperatures below 200 °C. Basically, the main problem was that the short circuit current was negligible in all cases. The best open circuit voltage was ~140 mV for the cell prepared from the CCTO target with [CuO]=11 at.%.

7.2. Perspectives.

To investigate the effect of thermal treatments on the cells (or Hall effect samples) at temperatures below 200 °C for longer times.

To perform rapid thermal annealing treatments to the solar cells at temperatures below 200 °C in vacuum or inert atmospheres such as Ar or N_2.

To investigate the use of a molybdenum front contact on the CCTO films, aiming to replace Cu (thermal expansion coefficient: 16.6×10^{-6} $m(mK)^{-1}$) due to its lower linear thermal expansion coefficient of 4.8×10^{-6} $m(mK)^{-1}$. This could be beneficial to the thermal treatments since it matches better that of the CdTe host (5.9 $m(mK)^{-1}$).

To use of indium as back contact of the solar cell, being this a reported ohmic contact on ZnO thin films with low rate of degradation upon time.

To fabricate heterojunction *p*-CCTO/n-ZnO solar cells at high substrate temperatures in order to decrease the defect density (such as interstitials and vacancies) of the films, and to produce an overall increase in crystallite and grain sizes.

EL JURADO DESIGNADO POR LA UNIDAD QUERÉTARO DEL CENTRO DE INVESTIGACIÓN Y DE ESTUDIOS AVANZADOS DEL INSTITUTO POLITÉCNICO NACIONAL, APROBÓ LA TESIS DE MAESTRÍA DEL (LA) C. ALEJANDRO GOJON MONTAÑEZ TITULADA: "CELDAS SOLARES DE HETEROUNIÓN BASADAS EN EL CUATERNARIO CuCdTeO FABRICADAS A TEMPERATURA AMBIENTE", FIRMAN AL CALCE DE COMÚN ACUERDO LOS INTEGRANTES DE DICHO JURADO, EN LA CIUDAD DE QUERÉTARO, QRO., A LOS VEINTINUEVE DÍAS DEL MES DE SEPTIEMBRE DE 2015.

DR. SERGIO JOAQUÍN JIMÉNEZ SANDOVAL

DRA. REBECA CASTANEDO PÉREZ

DR. ARTURO MENDOZA GALVÁN

CINVESTAV - IPN
Biblioteca Central

SSIT0013497